PASJ: Publ. Astron. Soc. Japan **59**, 487–506, 2007 June 25

Near-Infrared Imaging Polarimetry of the Star-Forming Region NGC 2024

Ryo KANDORI,[1] Motohide TAMURA,[1,2] Nobuhiko KUSAKABE,[2] Yasushi NAKAJIMA,[1] Takahiro NAGAYAMA,[5] Chie NAGASHIMA,[4] Jun HASHIMOTO,[1,3] Akika ISHIHARA,[2] Tetsuya NAGATA,[5] and James H. HOUGH[6]

[1]*National Astronomical Observatory, 2-21-1 Osawa, Mitaka, Tokyo 181-8588*
kandori@optik.mtk.nao.ac.jp

[2]*Graduate University for Advanced Studies, 2-21-1 Osawa, Mitaka, Tokyo 181-8588*

[3]*Department of Physics, Tokyo University of Science, 1-3 Kagurazaka, Shinjuku-ku, Tokyo 162-8601*

[4]*Department of Astrophysics, Nagoya University, Chikusa-ku, Nagoya 464-8602*

[5]*Department of Astronomy, Kyoto University, Sakyo-ku, Kyoto 606-8502*

[6]*Centre for Astrophysics Research, University of Hertfordshire, Hatfield, HERTS AL10 9AB, UK*

(Received 2006 November 7; accepted 2007 February 5)

Abstract

We conducted wide-field JHK_s imaging polarimetry toward NGC 2024, which is a massive star-forming region in the Orion B cloud. We found a prominent and extended polarized nebula over NGC 2024, and constrained the location of the illuminating source of the nebula through an analysis of polarization vectors. A massive star, IRS 2b with a spectral type of O8–B2, is located in the center of the symmetric vector pattern. Five small polarized nebulae associated with YSOs were discovered on our polarization images. These nebulae are responsible for the structures of circumstellar matter (i.e., disk/envelope systems) that produce strongly polarized light through dust scattering. For the point-like sources, we performed software aperture polarimetry in order to measure integrated polarizations, with which we detected candidate sources associated with circumstellar material. We found five young brown dwarfs with highly polarized integrated emission. These sources serve as direct evidence for the existence of a disk/envelope system around brown dwarfs. We investigated the fraction of highly polarized sources against the intrinsic luminosity of stars ($\propto$ mass), and found that the source detection rate remains constant from low luminosity (brown dwarfs) to higher luminosity (solar-type) stars. This result indicates that the relative disk scale-hight is rather independent of the stellar mass. We investigated the magnetic field structure of NGC 2024 through measurements of dichroic polarization. The average position angle of projected magnetic fields across the region is found to be 110°. We found a good consistency in magnetic field structures obtained using near-infrared dichroic polarization and sub-mm/far-infrared dust emission polarization, indicating that the dichroic polarizations at near-infrared wavelengths trace magnetic field structures inside dense ($A_V \lesssim 50$ mag) molecular clouds.

Key words: circumstellar matter — infrared: stars — ISM: individual (NGC 2024) — polarization — stars: formation

1. Introduction

NGC 2024 is a massive star-forming region in the Orion B giant molecular cloud at a distance of 415 pc (Anthony-Twarog 1982). In the optical images, NGC 2024 shows a bright nebulosity with a prominent central dark dust lane located in front of the ionized gas. Imaging observations at near-infrared wavelengths clearly revealed an embedded cluster in this region (e.g., Barnes et al. 1989; Lada et al. 1991; Haisch et al. 2001), which is high in stellar density (~ 400 stars pc^{-3}, Lada 1999) and is young in mean age (0.3 Myr, Meyer 1996). The structure of the H II region toward NGC 2024, forming at the edge of a molecular cloud, was studied in detail (Crutcher et al. 1986; Barnes et al. 1989). Though the dominant source of ionization powering the H II region has not been identified until recently, due to heavy obscuration by dust around the central region, Bik et al. (2003) suggested that the dominant source is IRS 2b, located 5″ north-west of IRS 2. They found that the spectral type of IRS 2b is in the range O8 V–B2 V, which is consistent with the intensities of radio continuum emission and recombination lines observed toward the H II region (Kruegel et al. 1982; Barnes et al. 1989). NGC 2024 includes a number of protostars forming along the "star forming ridge", a filamentary shaped dense molecular material, extending in the north–south direction. In the ridge, dense dust condensations, FIR 1–7, were reported based on 1.3 mm and 870 μm observations (Mezger et al. 1988, 1992).

The magnetic field structure of NGC 2024 was studied by observing linearly polarized thermal emission from aligned dust grains ($B_\perp$ measurements) and the Zeeman splitting of molecular or atomic lines ($B_\parallel$ measurements). Hildebrand et al. (1995) and Dotson et al. (2000) reported a far-infrared (100 μm) polarization map covering $\sim 3' \times 3'$ toward NGC 2024. They found that the overall magnetic field orientation is in the east–west direction. There is a local magnetic field structure at and around the star-forming ridge, but its detailed structure could not be resolved on their polarization vector map. Matthews, Fiege, and Moriarty-Schieven (2002) studied the magnetic field structure of the star-forming ridge in NGC 2024 based on sub-mm dust continuum observations using the polarimetry mode of JCMT/SCUBA. They revealed the detailed magnetic field

structure along the ridge, which is consistent with a previous 100 μm lower resolution polarization map. On the basis of their polarization map at 850 μm, they modeled the magnetic field structure of the star forming ridge as helical magnetic fields surrounding a curved filamentary cloud, and as magnetic field swept by the ionization front of the expanding H II region.

Crutcher et al. (1999) performed circular polarimetry toward NGC 2024 with the Very Large Array (VLA) to measure the Zeeman splitting of the absorption lines of H I and OH. They found that $B_{\parallel}$ smoothly varies from 0 μG in the northeast to ~ 100 μG in the southwest of the star-forming ridge, and suggested that the orientation of magnetic fields toward the lines of sight varies across the region.

At near-infrared wavelengths, the polarimetry of a few bright stars in NGC 2024 was reported (IRS 1: Wilking et al. 1980, IRS 1, 2: Heckert & Zeilik 1981). More recently, Moore and Yamashita (1994) conducted imaging polarimetry toward the infrared nebula associated with FIR 4. However, the field of view of their map was too small ($\sim 40'' \times 40''$) to reveal the polarization distribution over the entire surface of NGC 2024.

In this paper, we present polarization images of the NGC 2024 star-forming region, which is a part of our ongoing project of $JHK_{\rm s}$ polarimetry of star-forming regions. Our observations were sufficiently deep ($J = 19.2$ mag, $\mathrm{S/N} = 5$) and wide ($7\farcm7 \times 7\farcm7$), covering a large extent of NGC 2024. Near-infrared imaging polarimetry is particularly useful to trace polarized light from star-forming regions compared with that at optical wavelengths, where dust extinction is severe. Our wide-field $JHK_{\rm s}$ polarization images can be used to reveal large-scale infrared reflection nebulae (IRNe); to detect smaller scale IRNe associated with young stars that are responsible for the circumstellar material (e.g., disk/envelope system), producing strongly polarized light through dust scattering; and to delineate the magnetic field structure through measurements of dichroic polarization of point sources.

In section 2, we describe the observations and data reduction. We derived polarization maps of NGC 2024 and constrained the illuminating source of the large-scale IRNe through the polarization vector analysis described in subsection 3.1. In subsection 3.2, we present the newly found small-scale IRNe associated with young stars, and discuss their physical properties. In subsection 3.3, we present the results of software aperture polarimetry of point sources. The polarization properties of point sources are considered based on the measurements of both polarization degrees and colors due to dust extinction. In addition, we reveal the magnetic field structure over NGC 2024 obtained from the polarization angle of each source, and compare it with the data taken at other wavelengths. Our conclusions are summarized in section 4.

2. Observations and Data Reduction

We carried out near-infrared polarimetric observations of NGC 2024 using the imaging polarimeter SIRPOL (polarimetry mode of the SIRIUS camera: Kandori et al. 2006) on the 1.4 m telescope IRSF (Infrared Survey Facility) at the South African Astronomical Observatory (SAAO). SIRPOL consists of a single-beam polarimeter [rotating achromatic (1–2.5 μm) wave plate and high-extinction-ratio wiregrid analyzer] and the $JHK_{\rm s}$-simultaneous imaging camera SIRIUS (Nagayama 2003), which has three 1024×1024 HgCdTe infrared detectors (HAWAII array). IRSF/SIRPOL enables deep and wide-field ($7\farcm7 \times 7\farcm7$ with a scale of $0\farcs45$ pixel^{-1}) imaging polarimetry at $JHK_{\rm s}$ simultaneously. The polarizations of all of the 2MASS-detected sources (15.8, 15.1, and 14.1 mag at J, H, and $K_{\rm s}$, $\mathrm{S/N} = 10$) can be measured within an accuracy of 1%.

Observations were made on the night of 2006 February 13. The 1.25 μm (J), 1.63 μm (H), and 2.14 μm ($K_{\rm s}$) imaging polarimetry data of NGC 2024 were obtained simultaneously. We made 10 s exposures at 4 wave plate angles (in the sequence of 0°, 45°, 22.°5, and 67.°5) at 10 dithered positions (1 set). We repeated the same set 9 times toward the object. The sky frame was taken in the same manner. The total integration time toward NGC 2024 was 900 s per wave plate angle. The typical seeing during the observations was $\sim 1\farcs4$ (3 pixels) at J. We obtained twilight flat at the beginning and end of each night. In order to make good flat frames, we combined 23 sets of twilight flat observations (17 nights) taken during the period from 2005 December to 2006 February.

We processed the observed data in the same manner as described in Kandori et al. (2006) using the IRAF[1] (flat-field correction, median sky subtraction, and frame registration). Stokes I, Q, and U images were obtained using $I = (I_{0^\circ} + I_{22.^\circ5} + I_{45^\circ} + I_{67.^\circ5})/2$, $Q = I_{0^\circ} - I_{45^\circ}$, and $U = I_{22.^\circ5} - I_{67.^\circ5}$. The image of the polarization degree, P, and the polarization angle, θ, can be written as $P = \sqrt{Q^2 + U^2}/I$ and $\theta = 0.5 \times \arctan(U/Q)$. We calibrated the I sky level to be consistent with the surface brightness derived using 2MASS images covering a much larger field-of-view. The 10σ limiting magnitudes for the surface brightness of I were 19.6, 19.3, and 17.3 mag arcsec^{-2} for J, H, and $K_{\rm s}$, respectively. In figure 1 we show images of the $JHK_{\rm s}$-composite intensity (I) and the polarized intensity (PI). We note that the PSF of unpolarized stars is not perfectly canceled on the PI image, because the seeing size changes slightly during the observations to take Q and U.

For source detection and photometry on Stokes I images, we used the IRAF daophot package (Stetson 1987). We detected stars having a peak intensity greater than 10σ above the local sky background. The overlooked sources in automatic detection were collected by eye inspection. The detected numbers of sources were 240, 365, and 376 at J, H, and $K_{\rm s}$, respectively. We measured the instrumental magnitudes of stars by aperture photometry. The aperture radius was 3 pixels. The number of stars detected in all three bands with a photometric error of less than 0.1 mag was 211. The 10σ limiting magnitudes were 18.5, 18.0, and 16.5 mag for J, H, and $K_{\rm s}$, respectively. In order to obtain plate solutions, we matched the pixel coordinates of the detected sources and the celestial coordinates of their counterparts in the 2MASS Point-Source Catalog (Cutri et al. 2003), and applied the IRAF imcoords package to the matched list. The coordinate transformation error was $\sim 0\farcs1$ (rms). We performed a photometric calibration using the 2MASS-PSC.

[1] IRAF is distributed by the US National Optical Astronomy Observatories, which are operated by the Association of Universities for Research in Astronomy, Inc., under cooperative agreement with the National Science Foundation.

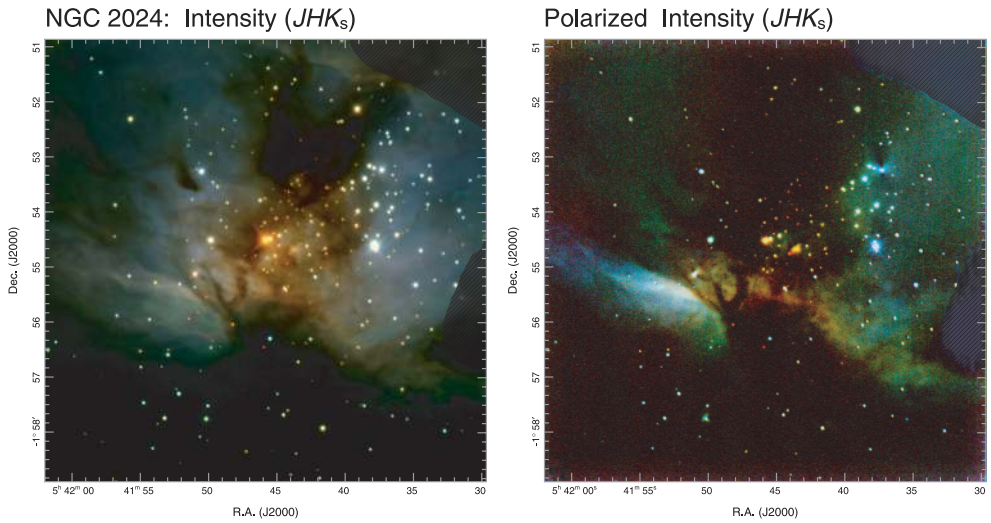

Fig. 1. Left: three-color composite of JHK_s intensity (I) images toward NGC 2024. Right: three-color composite of JHK_s polarized intensity (PI) images toward the same region. We note that there are bad pixel clusters on the J image around the upper-right corner and the middle of right side, both of which are masked by hatched line. The images are in logarithmic scale.

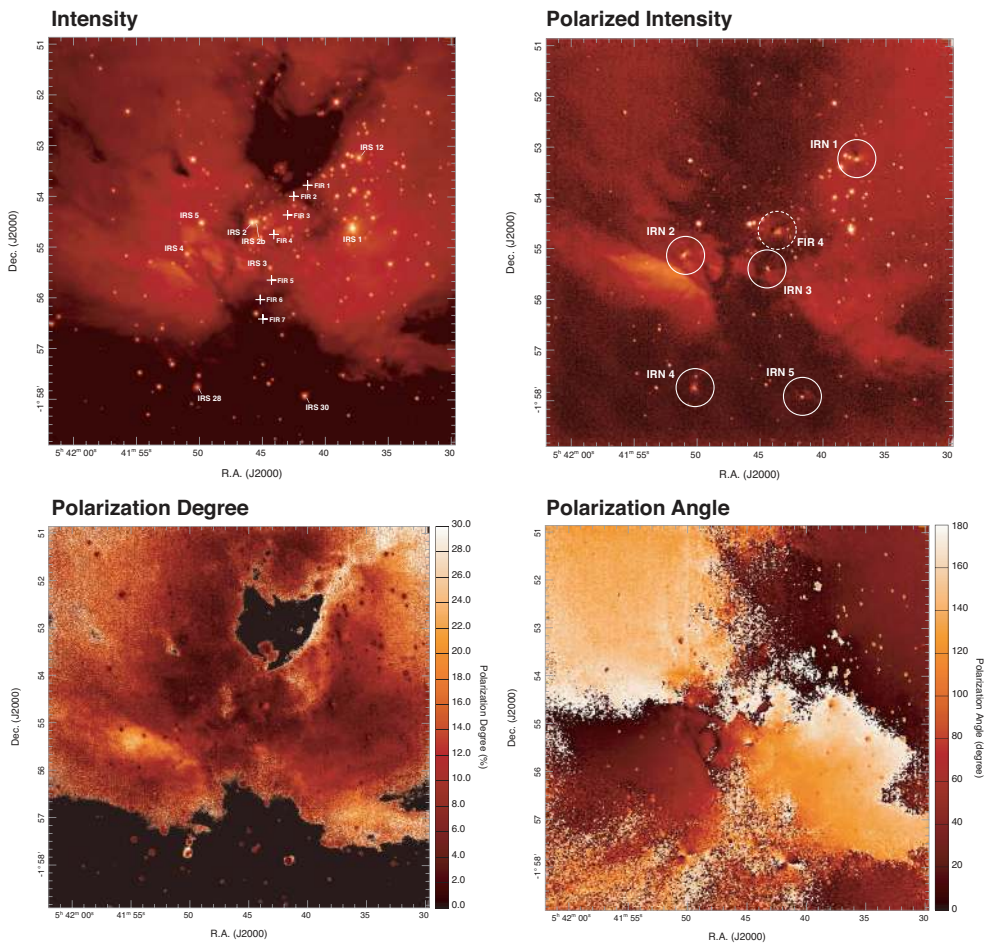

Fig. 2. Upper-left: Intensity (I) image of NGC 2024 in the H band (logarithmic scale). Plus symbols denote far-infrared sources (FIR 1–6: Mezger et al. 1988; FIR 7: Mezger et al. 1992). Some of bright stars are marked with cataloged IRS numbers in Barnes et al. (1989). Upper-right: Polarized intensity (PI) image of the same region (logarithmic scale). Newly found small infrared nebulae are enclosed by circles. A nebula enclosed by broken line circle was previously studied by infrared polarimetry (Moore & Yamashita 1995). Lower-left: Polarization degree (P) image. P_H is $\sim 30\%$ at maximum in the H band. The regions with low S/N ($I/\delta I < 10$) are masked. Lower-right: Polarization angle (θ_H) image.

The magnitude and color of our photometry were transformed into the 2MASS system using:

$$\mathrm{MAG_{2MASS}} = \mathrm{MAG_{IRSF}} + \alpha_1 \times \mathrm{COLOR_{IRSF}} + \beta_1, \quad (1)$$

$$\mathrm{COLOR_{2MASS}} = \alpha_2 \times \mathrm{COLOR_{IRSF}} + \beta_2, \quad (2)$$

where the coefficients α_1 are 0.029, -0.024, and 0.008 for J, H, and K_s, respectively. The coefficients α_2 for $J-H$ and $H-K_\mathrm{s}$ are 1.032 and 0.997, respectively. We note that the coefficients β_1 and β_2 include both the zero point and an aperture correction.

We carried out software aperture polarimetry of point sources on the combined intensity images for each wave plate angle ($I_{0°}$, $I_{22.5}$, $I_{45°}$, and $I_{67.5}$). This is because the center of point sources (i.e., aperture center) cannot be determined satisfactory on the Q and U images. We discuss the results in the H band, where nebula contamination is less than in the J band, and the scattering efficiency is higher than in the K_s band. Based on aperture photometry data of each angle image, the Stokes parameters for each source were derived as described above. The point sources on each angle image have a slightly different PSF due to varying seeing size (1.″3–1.″5 at J). We thus used different apertures for each image in order to measure the same fraction of stellar flux falling in the aperture. The adopted aperture sizes were 3.00, 3.24, 3.08, and 3.27 pixels for $I_{0°}$, $I_{22.5}$, $I_{45°}$, and $I_{67.5}$, respectively. The sky annulus was set to 10 pixels with 5 pixel width. Since the polarization degree, P, is a positive quantity, the derived P values tend to be overestimated, especially for low S/N sources. To correct the bias, we calculated the debiased P using $P_\mathrm{db} = \sqrt{P^2 - \delta P^2}$, where δP is the error in P (Wardle & Kronberg 1974).

3. Result and Discussion

3.1. Large-Scale Infrared Reflection Nebula (IRN)

Although near-infrared (H and K) polarimetry around a small nebula associated with FIR 4 was reported previously (Moore & Yamashita 1995), no wide-field polarimetry of NGC 2024 has been carried out. Our wide and deep observations with SIRPOL revealed the distribution of near-infrared polarization in NGC 2024 for the first time. In figure 2, we show the I, PI, P, and θ of NGC 2024 in the H band. The central dark lane running north–south is located in the foreground of the nebula, and obscures light from the H II region (figure 2: upper-left). In the same panel, we show the location of far-infrared sources (FIR 1–7, Mezger et al. 1988, 1992) associated with a filament of dense material, "star-forming ridge", located just behind the H II region. Among the far-infrared sources, FIR 4 is associated with a 2 μm source (Moore & Chandler 1989) as well as reflection nebula (Moore & Yamashita 1995), both of which are also confirmed with our data (see subsection 3.2). In addition to the large-scale IRN, there are smaller scale IRN associated with stars, which we discuss in the next section. We found prominent and extended *polarization* nebulosities over NGC 2024 for the first time (figure 2: upper-right). In contrast to the other regions, e.g., M 42, the exciting source of NGC 2024 has not been directly identified, due to heavy obscuration by the central dust lane. Although IRS 2 was thought to be the exciting source of NGC 2024 until recently (e.g., Grasdalen 1974), Bik et al. (2003) proposed that the dominant ionizing source of NGC 2024 is IRS 2b, located 5″ north-west of IRS 2 (figure 2: upper-left).

Our imaging polarimetry data can be used to constrain the location of ionizing source(s) of the nebula through a polarization vector analysis, assuming that the ionizing source and the illuminating source are the same. A vector map is shown in figure 3. We found that the vector patterns clearly appear to be centrosymmetric, and that the normal lines of each vector intersect at a position near the center of NGC 2024, shown by a white plus symbol ($\mathrm{RA} = 5^\mathrm{h}\ 41^\mathrm{m}45.^\mathrm{s}01, \mathrm{Dec} = -1°54'27.''7$). The location of the dominant illuminating source(s) of NGC 2024 is then determined to be located within the white circle (1σ error circle, radius $= 16.''7$) in figure 3. We note that the locations of both IRS 2 and IRS 2b are included in the error circle, but IRS 2b is closer to the center. The vector patterns at J, H, and K_s are consistent with each other, and result in the coincident symmetry center position. We colored polarization vectors black or green based on the angle θ between each vector and the line toward white plus symbol; vectors that seem to follow centrosymmetry, showing $\theta = 90° \pm 20°$, are in white, and other vectors are in green. Polarization vectors are mostly colored in white, indicating that most of the large-scale nebulosities are illuminated from star(s) in the central region enclosed by the white circle. The green vectors tend to be distributed over the north–south dark dust lane and around small-scale IRNe, which can be explained by superposition of the large-scale nebulosities and extra polarization fields, i.e., dichroic absorption of foreground materials and intrinsic polarization of small-scale IRNe.

3.2. Small-Scale IRN

We found five new small-scale IRNe (IRN 1–5) associated with stars that are shown in the *PI* image in figure 2. An object enclosed by dashed line circle is the IRN associated with FIR 4, which was studied previously by Moore and Yamashita (1995) by near-infrared polarimetry. We show *PI* and vector maps of IRNe in figure 4. It is clear that the pattern of the polarization vector appears to be centrosymmetric, indicating that the nebulosity is associated with the central star, and responsible for the structure of the circumstellar matter (e.g., disk/envelope systems) that produces strongly polarized light through dust scattering. The small nebulae in a larger-scale nebulosity or embedded in the cloud should be treated with caution, because the polarization toward such nebulae is a superposition of different polarization vectors (i.e., scattered light polarization and dichroic polarization). We subtracted the local background (constant value) around small-scale IRNe from the Stokes Q and U images in order to suppress the contribution from larger nebulosities. We determined the Q and U background levels at the position 20″ away from the center of IRN, and simply subtracted them from the original. We did not take the effect of dichroic polarization into account, because the resulting vector pattern of IRNe after subtraction of the local background was reasonably centrosymmetric, and an estimate of dichroic polarization is not straightforward.

All IRNe have certain structures on the *PI* images.

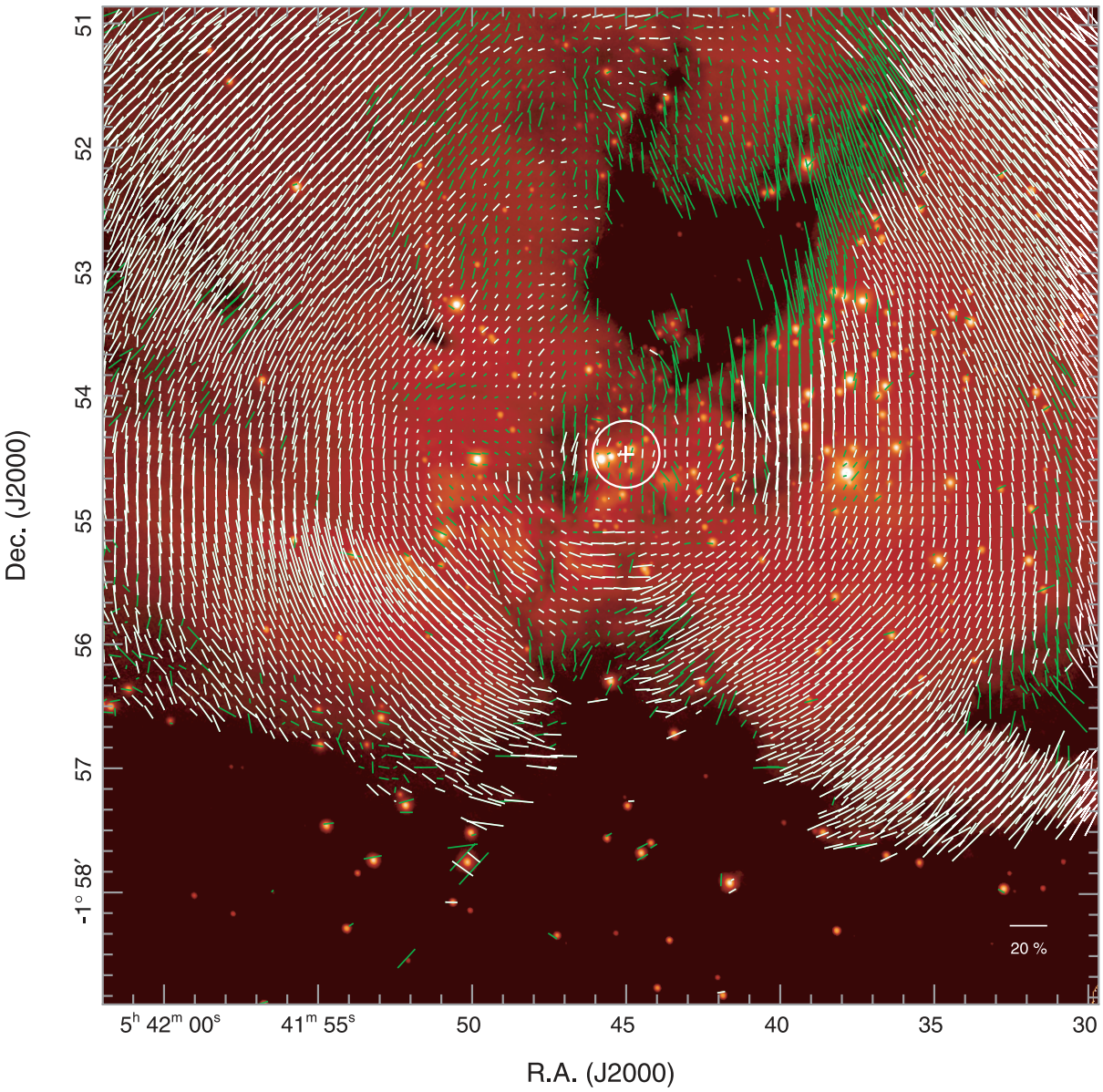

Fig. 3. Polarization vector map on the intensity image at H. White plus symbol indicates expected location of the illuminating source of NGC 2024. The white circle around the plus symbol denotes a 1σ error circle (see text). The polarization vectors on the low intensity region ($I/\delta I < 10$) are not plotted.

The spatial extent of small-scale IRNe is typically about 5000–10000 AU on the *PI* images, comparable to the size of "envelopes", rather "disks". IRNe show an elongated polarized emission pattern whose position angle is roughly 90°, 135°, 30°, 45°, and 135° for IRN 1–5, respectively. The emission pattern of IRN 1, 2, and 4 is clearly butterfly-shaped, and the dark lane extending perpendicular to the bright region can be seen in these IRNe. For IRN 3 and 5, the elongated emission pattern can only be seen on one side of the central star. These characteristics agree with the polarization picture of a disk/envelope system around young stars (e.g., Nagata et al. 1983; Hodapp 1984; Sato et al. 1985). The radiation from the star causes heavy extinction toward the direction of the disk (seen as a dark lane), but can escape toward the polar directions, and is then scattered by dust at the surface of the envelope, or a cavity created by the outflow (seen as a butterfly-shaped or monopolar IRN).

In figure 5, we show *PI* and vector maps of the IRN associated with FIR 4 in the J, H, and K_s bands. The counterpart of FIR 4 is best seen in the K_s band and located at (ΔRA, ΔDec) = ($7\farcs2$, $-7\farcs2$) in figure 5. Our vector maps show good agreement with those in the H and K bands reported by Moore and Yamashita (1995). The IRN appears as a monopolar shape with a position angle of $\sim 135°$, and shows a centrosymmetric vector pattern centered on FIR 4. The axis of IRN is consistent with that of the molecular outflow associated with FIR 4 (Chandler & Carlstrom 1996). The position angle of the polarization vector toward FIR 4 is $\sim 45°$, perpendicular to the axis of IRN, which is the general tendency in young stellar objects with IRN (see above).

In table 1, we summarize the observational properties of IRNe and its central stars. The polarization degree of each

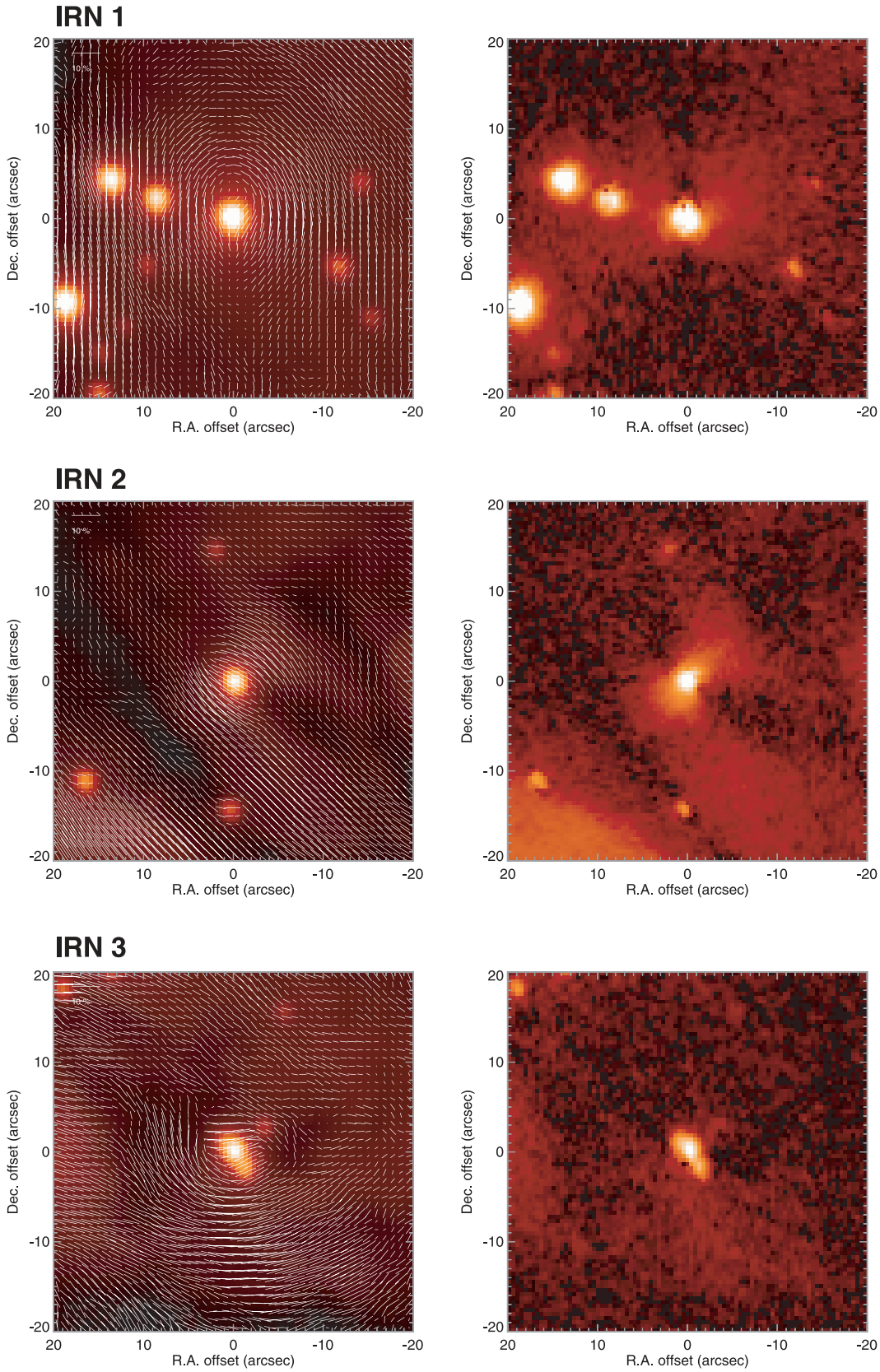

Fig. 4. Left column: Polarization vector maps on the I images of small IRNe in NGC 2024. The polarization vectors on the low intensity region (IRN 1–3: $I/\delta I < 10$, IRN 4–5: $I/\delta I < 5$) are not plotted. Right column: Polarized intensity images. All of the images are in the H band and on the logarithmic scale.

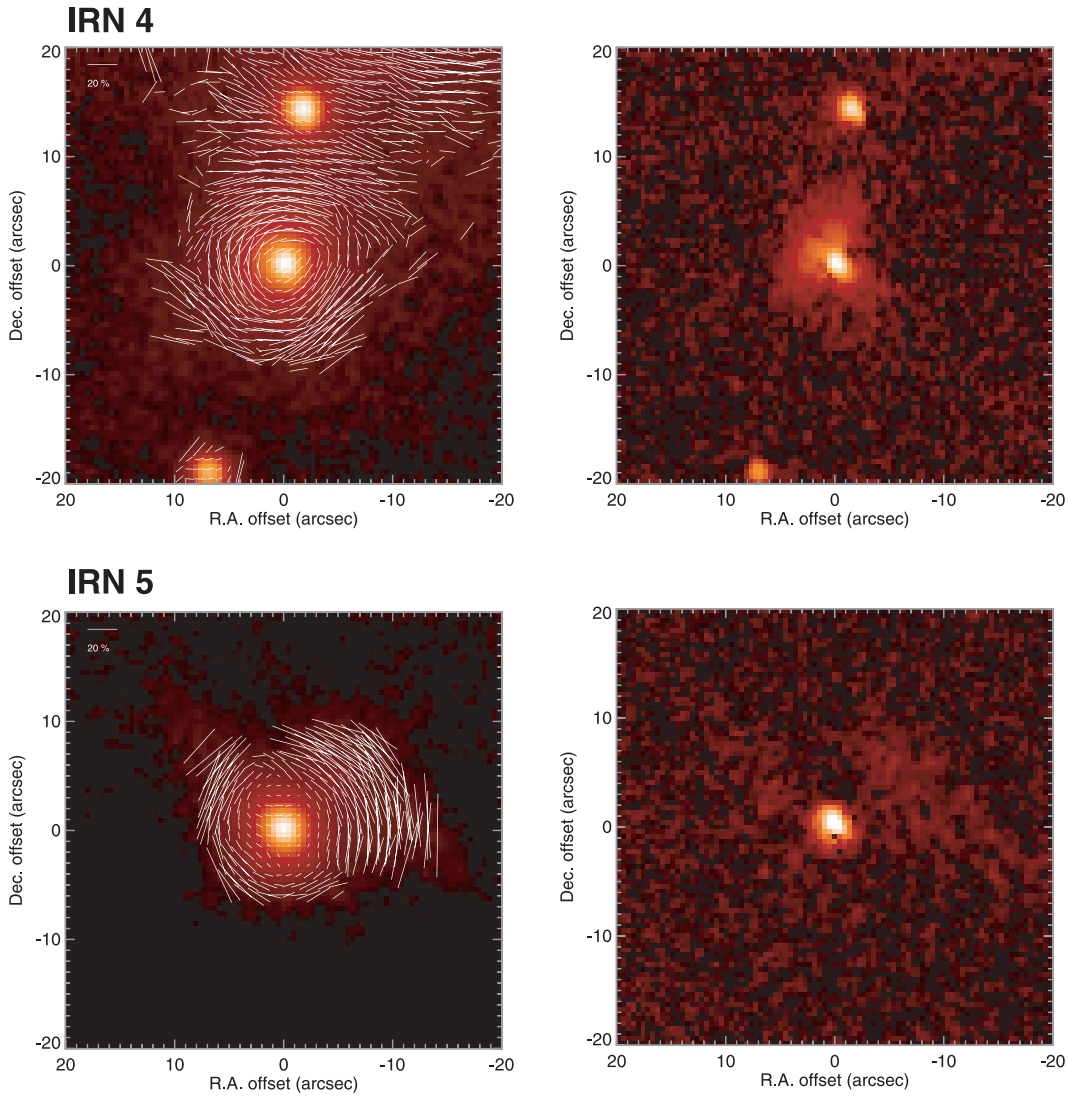

Fig. 4. (Continued.)

IRN (columns 4–6th) is not large, because unpolarized light from the H II region (e.g., free–free ionized gas emission) dilutes the polarized light. If we subtract the background intensity around IRN, the polarization degrees increase to a level comparable with typical reflection nebulae in other star-forming regions, as shown in parentheses. The IRN 1–5 are associated with stars IRS 12, 4, 3, 28 and 30, respectively. From their near-infrared colors, we found that the central stars of five IRNe are young, especially in a pre–main-sequence phase. The infrared color of the five sources was investigated in the $JHKLN$ bands by Haisch et al. (2001). Based on 2.2–10 μm spectral index α ($= d \log \lambda F_\lambda / d \log \lambda$) measurements, five sources, IRS 12 (IRN 1), IRS 4 (IRN 2), IRS 3 (IRN 3), IRS 28 (IRN 4), and IRS 30 (IRN 5), were classified into Class II, Class I, Class II, Class II, and Flat spectrum, respectively. This is consistent with the fact that they are accompanied by nebulous circumstellar materials. Following the method described in section 2, we performed aperture polarimetry of the central stars (columns 13–14). Except for the saturated source IRS 12 and the source IRS 3 with faint IRN, we found that the polarization vector angle, θ, of stars is roughly perpendicular to the major axis of IRN (column 3). This characteristic is in good agreement with those for young stellar objects accompanied by IRNe. These sources serve as good targets for future studies at higher resolution and at various wavelengths (e.g., large Opt–IR telescopes, ALMA) as well as in theoretical modeling.

3.3. *Aperture Polarimetry of Point-like Sources*

We performed software aperture polarimetry of point-like sources in order to measure the integrated polarization of possible unresolved nebulae. Our photometry and polarimetry of 211 stars with JHK_s detections are listed in table 2. The polarization vectors in the J, H, and K_s bands are quite consistent with each other. For the sources with $\delta\theta_\lambda$ of less than 3° (63 sources), the correlation coefficients for (θ_H, θ_J) and (θ_H, θ_{K_s}) are 0.99 and 0.98, respectively. The mean of the difference in θ_λ is small, which is $-1\overset{\circ}{.}4$ for $\langle\theta_H - \theta_J\rangle$ and $-1\overset{\circ}{.}7$ for $\langle\theta_H - \theta_{K_s}\rangle$. For sources with $P_\lambda/\delta P_\lambda$ of greater than 10 (64 sources), the linearly fitted slopes of P_H vs. P_J and

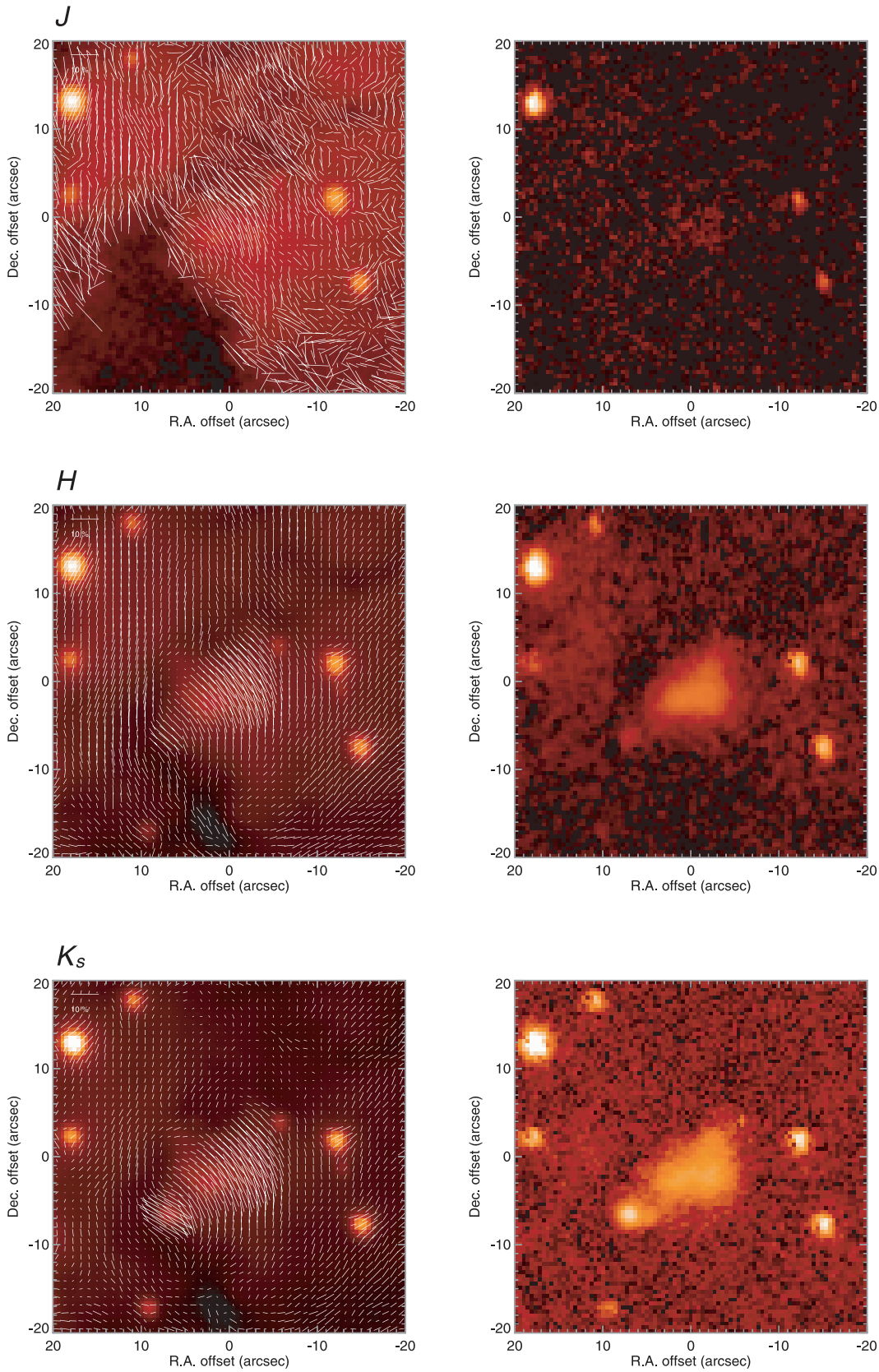

Fig. 5. Left column: Polarization vector maps superposed on the I images of $40'' \times 40''$ region around FIR 4. The polarization vectors on the low intensity region ($I/\delta I < 10$) are not plotted. Right column: Polarized intensity images. The images are on the logarithmic scale.

Table 1. Properties of small-scale IRNe.

Nebulae						Central Stars							
ID	Size* (AU)	PA* (°)	$P_{J,\max}$† (%)	$P_{H,\max}$† (%)	$P_{K_{s,\max}}$† (%)	No.‡	Name§	J‖ (mag)	H‖ (mag)	K_s‖ (mag)	Class#	P_H (%)	θ_H (°)
IRN 1	10000	90	12.5(19.0)	9.0(15.0)	—	—	IRS 12	10.36	9.33	8.63	II	—	—
IRN 2	7000	135	16.5(24.0)	14.5(21.0)	8.0(10.0)	138	IRS 4	12.45	10.49	9.19	I	8.1 ± 0.11	57 ± 0.4
IRN 3	6000	30	—	13.0(22.0)	9.0(12.0)	148	IRS 3	13.66	11.34	9.81	II	7.0 ± 0.10	104 ± 0.4
IRN 4	5000	45	28.0(30.0)	27.0(29.0)	—	191	IRS 28	13.95	11.85	10.62	II	5.1 ± 0.06	127 ± 0.4
IRN 5	6000	135	—	28.0(28.0)	—	194	IRS 30	12.59	10.48	9.32	Flat spectrum	1.5 ± 0.02	85 ± 0.3

* Size and position angle of IRNe on the *PI* image. The size of the nebula having intensity greater than 10σ above background was measured as the size of the IRN. The position angle denotes the orientation of polarized nebulosity of each IRN.

† Maximum polarization degree of IRNe was measured after the subtraction of local background on Q and U images. If we further remove the contribution from large-scale nebula by subtracting the local background intensity (I), the polarization degree of IRNe increases as shown in parentheses.

‡ Source number in table 2.

§ Star-ID based on Barnes et al. (1989).

‖ Magnitudes taken from 2MASS Point Source Catalog (Cutri et al. 2003).

Evolutionary state of the central stars (YSOs) based on the 2.2–10 μm spectral index measurements (Haisch et al. 2001).

P_H vs. P_{K_s} diagrams are 1.52 and 0.50, with the correlation coefficients of 0.98 and 0.91, respectively. These slopes are consistent with the empirical values of 1.61 and 0.61 from the relation $P \propto \lambda^{-\alpha}$, where $\alpha = 1.8 \pm 0.2$ (Whittet 1992). In the following, we discuss the aperture polarimetry results in the H band, where nebula contamination is less than in the J band, and the scattering efficiency is higher than in the K_s band.

3.3.1. Highly polarized sources (HPS)

We can detect candidate stars with intrinsic polarization (i.e., with circumstellar material) by selecting sources with larger polarizations than values estimated from the dichroic absorption due to foreground material. Firstly, we made two-color diagram for all of the sources detected in the JHK_s bands in order to classify the sample into three groups of dwarf+giant, PMS stars, and protostars. The result is shown in figure 6a. We found 143 stars in the dwarf+giant star region (filled circle), 63 stars in the PMS star region (open diamond), and 5 stars located on the right to the PMS region, i.e., the protostar region (open circle). We plotted these sources in the $H - K_s - 0.15$ versus P_H diagram shown in figure 6b. The value of 0.15 mag is the mean intrinsic color of stars (mostly G to M dwarfs) toward the object, calculated using the Galaxy model (Wainscoat et al. 1992; Cohen 1994), so that the horizontal axis of figure 6b corresponds to the mean E_{H-K_s}. The dashed line denotes the mean relationship between extinction and polarization for interstellar molecular clouds, $P_K(\%) = 2.23\tau_K^{3/4}$, from Jones (1989). A linear least absolute deviation fitting to our $H - K_s - 0.15$ and P_H data resulted in $P_H = 4.21 \times E_{H-K_s} = 1.69 \times A_H$ (solid line), where we forced the intercept value to be zero in the fitting. Our fitting result shows a similar relationship to the relation from Jones (1989). The polarization of stars with $P_H/A_H \sim 1.69$ is dominated by dichroic polarization produced by aligned interstellar dust grains. Observational upper limit of the relationship (dot-dashed line) can be described using the equation $P_{K,\max} = \tanh(\tau_p)$, where $\tau_p = (1-\eta)\tau_K/(1+\eta)$ when the parameter η is set to 0.875 (Jones 1989).

The sources with larger P_H/A_H values can be better candidates to show excess (intrinsic) polarizations, and hense good targets for further observations in order to study circumstellar materials around stars. We calculated P_H/A_H for each star, where A_H was measured on the two-color diagram (figure 6a). The histogram of P_H/A_H is shown in figure 7 (p.501). In the histogram, there is a clear peak around $P_H/A_H \sim 1.69$, which corresponds to the sources mainly affected by interstellar polarization. We found that the dwarf+giant stars (filled circle) and PMS stars (open diamond) show similar distribution in figure 6b. If we regard the stars with $P_H/A_H \geq 3.38$, two-times larger P_H/A_H than that for the interstellar polarization, as highly polarized sources (HPS), the fractions of HPS are 32%, 31%, and 35% for all the stars, dwarf+giant stars, and, PMS stars, respectively. The protostar candidates are not included in these statistics, because their intrinsic colors are not known. It is an interesting result that there is no tendency of higher polarization in earlier evolutionary stages or larger infrared excess. However, since a part of the locus of classical T Tauri stars overlaps with the reddening band, some fraction of PMS stars can be included in the sample of dwarf+giant stars. Thus, the HPS fraction for the dwarf+giant group may cause significant contamination from PMS stars, and caution must be applied.

3.3.2. Stellar mass versus P_H/A_H

It is of particular interest to investigate the fraction of HPS against the luminosity of stars ($\propto$ mass), because the information should be closely related to the dependence of the population of stars with a circumstellar disk on the mass of stars. Though the probabilities of disk inclination, orientation, and suffered extinction from foreground materials are expected to be random, other factors, like the shape (scale height) and evolutional timescale (lifetime) of disk, may have some dependence on the stellar mass.

It is likely that the effect of the disk lifetime on the detection ratio of HPS is not significant. As shown in figure 6a, many sources are located in the Class II region in the two-color diagram. By using a J–H vs. K–L diagram, Haisch et al. (2000) reported that infrared excess stars (Class II and protostars) occupy $\sim 80\%$ fraction of the stellar population in this region. Since the age of most sources could be younger than, or comparable with, the disk lifetime (~ 10 Myr, Strom et al. 1993), the observed HPS fraction should not be affected

Table 2. Polarizations of point-like sources in NGC 2024.

No.	HPS ID*	RA† (h m s)	Dec† (° ′ ″)	J (mag)	H (mag)	K_s (mag)	P_H (%)	A_H‡ (mag)	P_H/A_H§ (% mag^{-1})	θ_H (°)
1	—	5 41 47.25	−1 51 08.3	17.64	15.84	14.75	3.25±1.62	1.24	2.63±1.31	5±12.8
2	—	5 41 46.95	−1 51 09.9	15.48	13.79	12.98	3.50±0.30	1.67	2.09±0.18	19± 2.4
3	—	5 41 44.65	−1 51 12.5	16.87	14.50	13.26	5.47±0.70	2.71	2.02±0.26	50± 3.6
4	—	5 41 58.52	−1 51 12.9	14.84	13.09	12.28	2.06±0.09	1.64	1.25±0.05	87± 1.2
5	HPS 1	5 41 50.10	−1 51 18.1	16.01	14.84	14.03	1.56±0.43	0.33	4.75±1.32	84± 7.7
6	—	5 41 45.64	−1 51 22.8	14.74	12.74	11.68	2.44±0.11	2.23	1.09±0.05	74± 1.3
7	—	5 41 57.86	−1 51 27.9	13.52	12.31	11.80	0.30±0.04	0.90	0.34±0.05	83± 4.1
8	—	5 41 48.31	−1 51 30.5	17.50	15.53	14.39	2.82±1.51	1.51	1.86±1.00	164±13.5
9	—	5 41 43.68	−1 51 35.3	15.28	12.78	11.61	1.32±0.10	2.48	0.53±0.04	33± 2.1
10	—	5 41 43.89	−1 51 39.8	17.79	14.27	12.57	1.58±0.35	3.78	0.42±0.09	50± 6.2
11	—	5 41 37.30	−1 51 40.3	15.56	12.84	11.35	3.24±0.26	3.27	0.99±0.08	152± 2.3
12	—	5 41 45.09	−1 51 44.3	14.21	11.60	10.29	4.25±0.05	2.93	1.45±0.02	44± 0.3
13	—	5 41 39.02	−1 51 45.3	15.06	12.81	11.73	4.16±0.14	2.38	1.75±0.06	141± 0.9
14	—	5 41 41.77	−1 51 45.6	13.93	12.35	11.63	1.31±0.07	1.41	0.93±0.05	164± 1.4
15	—	5 41 54.73	−1 51 46.2	17.68	16.04	15.02	2.39±1.37	1.02	2.33±1.34	138±14.2
16	—	5 41 46.52	−1 51 48.8	17.66	15.29	13.84	3.80±0.87	1.95	1.95±0.45	57± 6.4
17	—	5 41 38.08	−1 51 53.6	18.04	15.91	14.65	5.62±1.55	1.70	3.31±0.91	169± 7.6
18	—	5 41 45.38	−1 51 56.6	17.91	13.81	11.42	11.96±0.25	4.23	2.83±0.06	28± 0.6
19	—	5 41 41.03	−1 51 57.7	17.34	13.79	12.14	4.26±0.35	3.69	1.15±0.09	26± 2.3
20	—	5 41 37.26	−1 51 57.9	17.20	14.88	13.67	4.62±0.37	2.62	1.76±0.14	161± 2.3
21	—	5 41 51.70	−1 52 08.2	15.16	13.14	11.88	2.49±0.13	1.49	1.67±0.08	98± 1.4
22	—	5 41 35.37	−1 52 11.5	14.83	12.70	11.40	3.12±0.16	1.65	1.89±0.10	144± 1.5
23	HPS 2	5 41 32.83	−1 52 12.5	14.29	12.65	11.65	7.04±0.07	1.02	6.88±0.06	131± 0.3
24	—	5 41 45.77	−1 52 13.0	16.46	13.91	12.37	3.05±0.53	2.17	1.40±0.24	63± 4.9
25	—	5 41 34.52	−1 52 13.4	15.39	14.12	13.40	2.91±0.62	1.37	2.11±0.45	145± 5.9
26	—	5 41 51.61	−1 52 16.7	14.48	12.91	12.17	0.60±0.13	1.49	0.40±0.08	131± 5.9
27	—	5 41 55.68	−1 52 18.6	12.77	10.29	9.17	1.46±0.01	2.25	0.65±0.01	144± 0.3
28	HPS 3	5 41 31.86	−1 52 19.9	12.31	10.97	10.45	2.56±0.02	0.72	3.56±0.03	127± 0.2
29	—	5 41 48.06	−1 52 19.9	15.90	14.14	13.24	2.91±0.29	1.84	1.58±0.16	46± 2.9
30	—	5 41 40.27	−1 52 20.5	15.40	12.66	11.26	2.18±0.11	3.14	0.70±0.03	159± 1.4
31	—	5 41 40.52	−1 52 21.2	16.52	13.49	11.85	2.22±0.25	3.68	0.60±0.07	165± 3.2
32	—	5 41 50.90	−1 52 23.6	15.63	14.34	13.55	0.85±0.31	0.59	1.44±0.52	44± 9.7
33	—	5 41 35.46	−1 52 28.8	13.27	11.51	10.51	3.02±0.03	2.06	1.47±0.01	150± 0.3
34	—	5 41 48.94	−1 52 29.7	16.12	13.77	12.60	4.09±0.19	2.59	1.58±0.07	72± 1.4
35	—	5 41 37.49	−1 52 31.0	16.32	14.75	13.81	3.21±1.46	0.96	3.33±1.52	161±11.8
36	—	5 41 31.62	−1 52 31.6	14.32	13.12	12.52	1.70±0.13	1.09	1.57±0.12	122± 2.2
37	—	5 41 36.94	−1 52 33.2	13.16	11.64	10.93	2.36±0.06	1.43	1.65±0.04	154± 0.7
38	—	5 41 36.86	−1 52 37.5	14.16	12.74	11.96	2.02±0.20	1.48	1.36±0.14	165± 2.9
39	—	5 41 51.40	−1 52 41.0	17.01	15.03	13.76	2.30±0.57	1.38	1.66±0.41	70± 6.9
40	—	5 41 36.70	−1 52 42.9	13.24	11.94	11.40	2.07±0.11	0.98	2.11±0.11	169± 1.5
41	—	5 41 48.08	−1 52 43.0	18.06	15.80	14.52	1.32±1.30	1.90	0.69±0.69	77±20.1
42‖	—	5 41 49.29	−1 52 44.3	17.81	15.87	14.34	1.02±1.45	—	—	133±23.4
43	—	5 41 37.40	−1 52 44.6	13.41	11.87	11.10	3.27±0.10	1.50	2.18±0.07	167± 0.9
44	HPS 4	5 41 36.74	−1 52 44.9	13.93	12.69	12.21	2.94±0.18	0.62	4.77±0.29	11± 1.7
45	—	5 41 51.47	−1 52 47.1	15.51	13.91	12.99	1.96±0.36	1.03	1.91±0.35	80± 5.2
46	—	5 41 48.23	−1 52 48.3	16.50	14.53	13.50	2.44±0.45	2.16	1.13±0.21	53± 5.1
47	—	5 41 46.79	−1 52 54.7	16.89	15.02	13.99	5.52±1.42	2.11	2.61±0.67	65± 7.1
48	—	5 41 49.83	−1 52 56.1	15.63	13.11	11.67	1.56±0.12	2.24	0.69±0.05	65± 2.2
49	—	5 41 50.68	−1 53 06.5	16.20	14.73	13.74	<0.86	0.72	<1.20	83±60.4
50	—	5 41 33.86	−1 53 08.7	13.71	12.47	11.81	2.50±0.17	1.20	2.08±0.14	136± 1.9
51	HPS 5	5 41 38.25	−1 53 09.1	12.00	10.07	9.17	8.45±0.04	1.90	4.45±0.02	4± 0.2
52	—	5 41 36.38	−1 53 09.3	15.39	13.84	13.05	4.32±0.36	1.57	2.75±0.23	174± 2.4
53	HPS 6	5 41 37.90	−1 53 11.2	11.92	10.50	9.86	4.37±0.09	1.23	3.57±0.07	0± 0.6
54‖	—	5 41 50.88	−1 53 12.8	15.63	13.99	12.70	1.75±1.12	—	—	81±15.4

Table 2. (Continued.)

No.	HPS ID*	RA† (h m s)	Dec† (° ′ ″)	J (mag)	H (mag)	K_s (mag)	P_H (%)	A_H‡ (mag)	P_H/A_H§ (% mag^{-1})	θ_H (°)
55	—	5 41 37.98	−1 53 18.7	15.93	14.09	12.99	2.51±1.14	1.30	1.93±0.88	7±11.8
56	—	5 41 36.54	−1 53 18.8	14.72	12.93	12.02	3.94±0.29	1.88	2.10±0.15	163± 2.1
57	HPS 7	5 41 34.41	−1 53 19.5	12.72	11.16	10.44	5.22±0.05	1.45	3.60±0.03	118± 0.3
58	—	5 41 30.25	−1 53 20.3	14.96	13.64	12.91	2.99±0.21	1.35	2.22±0.16	141± 2.0
59	—	5 41 33.83	−1 53 23.4	11.84	10.28	9.39	1.14±0.02	1.79	0.64±0.01	129± 0.6
60	—	5 41 36.30	−1 53 24.4	16.39	14.42	13.21	2.27±0.72	1.44	1.57±0.50	166± 8.6
61	—	5 41 43.49	−1 53 24.6	16.48	13.63	12.05	3.05±0.37	2.72	1.12±0.14	85± 3.4
62	—	5 41 30.89	−1 53 24.6	14.21	12.97	12.29	3.68±0.11	1.24	2.97±0.09	131± 0.9
63	HPS 8	5 41 38.14	−1 53 25.5	17.27	15.27	14.20	10.10±3.24	2.25	4.49±1.44	172± 8.7
64	—	5 41 39.49	−1 53 26.9	13.57	10.93	9.61	7.49±0.08	2.98	2.51±0.03	169± 0.3
65	—	5 41 49.67	−1 53 27.0	14.67	12.82	11.87	2.50±0.39	1.97	1.27±0.20	101± 4.4
66	HPS 9	5 41 38.32	−1 53 28.4	16.56	14.29	13.18	11.06±1.15	2.47	4.47±0.47	179± 3.0
67	—	5 41 35.03	−1 53 28.7	14.27	13.02	12.38	2.33±0.14	1.17	1.99±0.12	129± 1.7
68	—	5 41 43.92	−1 53 29.2	17.82	14.17	12.32	8.32±0.87	4.35	1.92±0.20	63± 3.0
69	—	5 41 49.64	−1 53 29.3	15.69	14.11	13.49	2.11±1.05	1.03	2.05±1.02	106±12.8
70	—	5 41 49.38	−1 53 31.1	14.88	13.03	12.04	3.20±0.37	2.04	1.57±0.18	75± 3.3
71	—	5 41 49.31	−1 53 32.7	14.84	13.02	12.09	2.59±0.30	1.93	1.34±0.16	85± 3.3
72	—	5 41 38.33	−1 53 33.0	13.44	12.89	12.53	0.94±0.27	0.00	—	121± 8.0
73	—	5 41 39.50	−1 53 33.6	15.18	12.54	11.10	6.95±0.15	3.22	2.15±0.05	169± 0.6
74	—	5 41 40.20	−1 53 34.1	15.12	11.98	10.02	8.21±0.27	2.88	2.85±0.09	168± 0.9
75	—	5 41 40.06	−1 53 35.5	15.40	12.59	11.16	10.06±0.36	3.22	3.13±0.11	169± 1.0
76	—	5 41 35.91	−1 53 37.1	15.48	14.12	13.33	2.31±0.52	0.72	3.23±0.73	153± 6.3
77	—	5 41 34.02	−1 53 38.8	15.28	14.01	13.31	2.15±0.36	1.28	1.68±0.28	150± 4.7
78	—	5 41 36.32	−1 53 39.3	14.08	12.30	11.33	2.90±0.12	1.98	1.46±0.06	156± 1.2
79	—	5 41 36.94	−1 53 39.3	14.78	12.78	11.60	2.44±0.23	1.52	1.61±0.15	164± 2.7
80	—	5 41 45.86	−1 53 44.8	16.50	13.89	12.47	1.97±0.95	3.10	0.63±0.31	68±12.4
81	—	5 41 51.17	−1 53 45.9	15.35	13.51	12.50	5.67±0.44	2.07	2.74±0.21	92± 2.2
82	—	5 41 33.03	−1 53 46.5	15.97	14.26	13.37	1.55±0.34	1.81	0.85±0.19	127± 6.1
83	—	5 41 46.21	−1 53 46.7	14.06	11.25	10.00	2.33±0.10	2.68	0.87±0.04	82± 1.2
84	—	5 41 40.63	−1 53 48.2	17.70	14.62	12.81	7.89±1.39	2.92	2.70±0.48	154± 5.0
85	HPS 10	5 41 35.76	−1 53 48.3	16.34	14.94	14.16	14.45±0.85	1.47	9.83±0.58	112± 1.7
86	—	5 41 48.61	−1 53 49.5	15.09	12.64	11.47	4.60±0.22	2.58	1.78±0.08	64± 1.4
87	—	5 41 33.98	−1 53 51.0	13.72	12.07	11.21	3.05±0.10	1.73	1.76±0.06	136± 0.9
88‖	—	5 41 43.91	−1 53 51.3	16.85	14.80	13.15	0.89±0.83	—	—	58±19.5
89	—	5 41 56.80	−1 53 52.1	14.06	11.98	11.06	4.67±0.03	1.73	2.70±0.02	51± 0.2
90	—	5 41 41.38	−1 53 52.2	17.80	13.77	11.77	4.35±0.27	4.68	0.93±0.06	150± 1.8
91	HPS 11	5 41 36.60	−1 53 54.4	11.90	10.25	9.55	4.05±0.03	1.17	3.46±0.02	146± 0.2
92	HPS 12	5 41 34.03	−1 53 55.9	15.66	14.35	13.55	3.18±0.58	0.60	5.26±0.96	147± 5.1
93	HPS 13	5 41 38.08	−1 53 57.2	13.75	11.58	10.58	7.22±0.07	2.02	3.57±0.04	162± 0.3
94	HPS 14	5 41 31.70	−1 53 57.3	12.53	11.14	10.56	4.66±0.04	0.88	5.27±0.04	127± 0.2
95	HPS 15	5 41 39.09	−1 53 58.4	12.30	10.14	8.94	10.21±0.02	2.55	4.00±0.01	171± 0.0
96	—	5 41 36.82	−1 53 58.9	12.69	11.03	10.16	3.47±0.04	1.74	1.99±0.02	140± 0.3
97	HPS 16	5 41 39.25	−1 54 02.2	16.50	14.41	13.14	10.81±0.51	1.61	6.70±0.32	178± 1.3
98	—	5 41 42.54	−1 54 02.9	16.79	13.73	11.92	4.19±0.53	2.87	1.46±0.19	112± 3.6
99	HPS 17	5 41 31.39	−1 54 05.1	14.00	12.75	12.24	3.77±0.12	0.87	4.31±0.14	128± 0.9
100	—	5 41 45.06	−1 54 06.4	18.24	13.06	10.27	2.55±0.15	6.70	0.38±0.02	62± 1.7
101	—	5 41 36.69	−1 54 08.2	13.51	11.76	11.01	3.81±0.07	1.29	2.95±0.05	141± 0.5
102	HPS 18	5 41 49.08	−1 54 08.6	14.25	12.98	12.16	5.13±0.27	0.51	10.12±0.53	106± 1.5
103	—	5 41 42.49	−1 54 09.8	15.06	12.63	11.41	2.07±0.46	2.69	0.77±0.17	131± 6.2
104	—	5 41 45.90	−1 54 11.1	17.13	13.14	11.07	6.55±0.19	4.85	1.35±0.04	76± 0.8
105	HPS 19	5 41 39.19	−1 54 14.1	14.39	11.43	9.70	9.34±0.05	2.75	3.39±0.02	171± 0.2
106	—	5 41 36.67	−1 54 15.1	17.11	15.12	13.98	2.43±1.21	1.55	1.57±0.78	155±12.8
107	—	5 41 48.68	−1 54 15.8	16.30	13.47	11.88	5.93±0.46	2.66	2.23±0.17	73± 2.2
108	—	5 41 32.36	−1 54 19.4	17.08	15.23	13.94	3.24±1.62	1.12	2.89±1.44	113±12.8

Table 2. (Continued.)

No.	HPS ID*	RA† (h m s)	Dec† (° ′ ″)	J (mag)	H (mag)	K_s (mag)	P_H (%)	A_H‡ (mag)	P_H/A_H§ (% mag^{-1})	θ_H (°)
109	—	5 41 44.36	−1 54 20.3	16.16	13.02	11.39	3.21±1.23	3.71	0.86±0.33	156± 10.2
110	HPS 20	5 41 35.83	−1 54 22.1	16.37	14.71	13.61	4.45±1.82	0.94	4.76±1.95	150± 10.8
111	—	5 41 45.23	−1 54 22.9	16.64	13.14	11.29	<1.49	4.27	<0.35	17± 31.5
112	—	5 41 41.98	−1 54 24.0	15.37	12.27	10.47	5.71±0.20	2.96	1.93±0.07	132± 1.0
113	—	5 41 36.24	−1 54 24.2	12.18	10.20	8.90	4.19±0.02	1.34	3.13±0.02	121± 0.1
114	—	5 41 37.63	−1 54 24.6	13.00	11.26	10.49	3.01±0.09	1.48	2.03±0.06	148± 0.8
115	—	5 41 38.48	−1 54 25.6	12.01	11.31	11.15	0.74±0.29	0.00	—	107± 10.6
116	—	5 41 56.85	−1 54 26.3	15.90	13.76	12.66	6.93±0.18	2.35	2.95±0.08	57± 0.8
117	—	5 41 38.72	−1 54 29.2	16.55	14.24	12.76	1.79±2.09	1.77	1.01±1.18	8± 21.7
118	HPS 21	5 41 31.40	−1 54 34.7	16.02	14.28	13.21	7.43±0.75	1.15	6.46±0.65	130± 2.9
119	—	5 41 44.84	−1 54 35.8	15.97	12.79	10.91	3.44±0.65	3.06	1.13±0.21	8± 5.3
120	—	5 41 42.81	−1 54 36.2	14.74	11.95	10.63	2.40±0.20	2.88	0.83±0.07	130± 2.4
121	—	5 41 41.49	−1 54 39.3	15.91	12.71	11.00	5.28±0.47	3.89	1.36±0.12	128± 2.5
122	HPS 22	5 41 34.49	−1 54 41.1	12.11	10.70	10.12	4.40±0.03	0.85	5.17±0.03	109± 0.2
123	—	5 41 36.46	−1 54 41.2	15.35	13.79	12.95	4.03±0.64	1.65	2.44±0.39	109± 4.5
124	—	5 41 32.85	−1 54 44.3	13.71	12.72	12.20	2.55±0.11	0.86	2.99±0.13	119± 1.2
125	—	5 41 41.39	−1 54 44.6	18.41	13.65	11.40	5.39±0.40	5.30	1.02±0.08	126± 2.1
126	—	5 41 42.62	−1 54 45.8	15.38	12.36	10.86	4.52±0.34	3.45	1.31±0.10	128± 2.1
127	—	5 41 45.12	−1 54 47.1	15.41	11.79	9.70	1.22±0.41	3.64	0.34±0.11	137± 9.1
128	—	5 41 36.83	−1 54 47.9	14.55	12.77	11.86	5.26±0.36	1.87	2.81±0.19	119± 2.0
129	—	5 41 45.71	−1 54 49.4	15.63	13.04	11.46	<1.01	2.22	<0.46	84±150.5
130	HPS 23	5 41 34.57	−1 54 50.0	16.69	15.34	14.57	4.97±3.27	0.70	7.10±4.67	111± 15.7
131	—	5 41 51.11	−1 54 52.3	15.85	14.06	12.94	2.38±2.07	1.17	2.03±1.77	70± 18.8
132	HPS 24	5 41 31.86	−1 54 53.7	13.44	11.68	10.98	5.56±0.03	1.26	4.41±0.03	118± 0.2
133	—	5 41 38.19	−1 54 55.0	14.74	12.66	11.52	5.65±0.27	2.39	2.37±0.11	122± 1.4
134	—	5 41 45.96	−1 55 01.9	16.77	12.97	10.83	6.42±0.99	3.94	1.63±0.25	85± 4.4
135	—	5 41 42.45	−1 55 02.6	16.16	12.83	10.89	6.81±0.23	3.27	2.08±0.07	106± 0.9
136	—	5 41 45.32	−1 55 02.7	17.24	13.99	12.21	8.50±1.77	4.09	2.08±0.43	90± 5.8
137	—	5 41 45.69	−1 55 04.9	18.30	13.84	11.72	15.95±1.39	4.90	3.25±0.28	78± 2.5
138	HPS 25	5 41 50.97	−1 55 07.0	12.47	10.46	9.26	8.09±0.11	1.52	5.32±0.07	57± 0.4
139	—	5 41 55.78	−1 55 09.3	12.86	11.77	11.28	2.35±0.09	0.88	2.69±0.10	101± 1.0
140	—	5 41 42.20	−1 55 10.0	12.82	11.28	10.53	4.70±0.06	1.50	3.14±0.04	98± 0.4
141	HPS 26	5 41 33.47	−1 55 13.4	14.05	12.49	11.84	6.11±0.09	1.04	5.89±0.09	119± 0.4
142	HPS 27	5 41 53.88	−1 55 16.3	14.61	11.88	10.33	13.45±0.27	2.51	5.36±0.11	80± 0.6
143	—	5 41 52.09	−1 55 18.2	13.07	11.99	11.48	1.77±0.61	0.88	2.01±0.69	72± 9.3
144	HPS 28	5 41 34.87	−1 55 18.5	10.77	9.76	9.25	5.45±0.01	0.84	6.51±0.02	113± 0.1
145	HPS 29	5 41 31.94	−1 55 18.6	12.45	10.74	9.90	7.39±0.04	1.73	4.26±0.03	121± 0.2
146	—	5 41 40.60	−1 55 18.6	15.91	12.83	11.26	5.30±0.35	3.57	1.49±0.10	137± 1.9
147	HPS 30	5 41 51.00	−1 55 21.3	13.85	12.94	12.56	2.49±0.67	0.57	4.34±1.16	99± 7.4
148	HPS 31	5 41 44.40	−1 55 22.8	13.69	11.43	10.02	7.00±0.10	1.78	3.94±0.05	104± 0.4
149	—	5 41 44.33	−1 55 24.9	14.52	12.37	11.30	5.33±0.16	2.32	2.30±0.07	119± 0.9
150	HPS 32	5 41 31.47	−1 55 32.7	14.22	12.13	10.79	6.11±0.11	1.51	4.06±0.07	111± 0.5
151	HPS 33	5 41 38.22	−1 55 36.3	12.84	11.54	11.03	5.38±0.10	0.69	7.84±0.15	117± 0.5
152	HPS 34	5 41 34.43	−1 55 38.6	16.35	14.50	13.53	9.07±1.03	2.01	4.52±0.52	105± 3.2
153‖	—	5 41 34.76	−1 55 52.2	17.20	13.93	11.78	11.06±0.50	—	—	94± 1.3
154	—	5 41 56.68	−1 55 52.6	13.52	12.41	11.95	2.25±0.12	0.71	3.15±0.17	73± 1.5
155	HPS 35	5 41 36.39	−1 55 54.9	12.85	11.43	10.89	7.12±0.05	0.82	8.69±0.06	115± 0.2
156	—	5 41 51.43	−1 55 55.8	17.47	14.15	12.59	9.32±1.01	3.39	2.75±0.30	111± 3.1
157	—	5 41 54.30	−1 55 56.6	13.31	12.29	11.75	2.73±0.08	0.89	3.06±0.09	111± 0.8
158	—	5 41 38.41	−1 55 58.3	16.16	13.29	11.92	8.39±0.22	3.07	2.73±0.07	109± 0.8
159	HPS 36	5 41 38.77	−1 56 02.5	14.09	12.10	11.01	10.69±0.10	2.26	4.73±0.04	112± 0.3
160	HPS 37	5 41 33.72	−1 56 06.9	15.31	12.56	11.22	12.74±0.25	3.04	4.18±0.08	110± 0.6
161	HPS 38	5 41 35.43	−1 56 15.5	13.72	13.05	12.81	0.78±0.21	0.23	3.40±0.90	103± 7.3
162	HPS 39	5 41 45.50	−1 56 17.3	11.72	11.08	10.86	1.17±0.02	0.18	6.45±0.11	116± 0.5

Table 2. (Continued.)

No.	HPS ID*	RA† (h m s)	Dec† (° ′ ″)	J (mag)	H (mag)	K_s (mag)	P_H (%)	A_H‡ (mag)	P_H/A_H§ (% mag^{-1})	θ_H (°)
163	—	5 41 42.54	−1 56 17.7	13.82	12.22	11.46	4.98±0.09	1.56	3.18±0.06	116± 0.5
164	—	5 42 01.14	−1 56 21.4	13.80	12.63	12.13	2.11±0.07	0.86	2.46±0.08	85± 0.9
165	HPS 40	5 41 35.81	−1 56 22.3	16.06	13.08	11.37	13.79±0.42	2.85	4.84±0.15	118± 0.9
166	—	5 41 39.06	−1 56 26.5	16.42	13.14	11.42	6.79±0.54	3.94	1.72±0.14	77± 2.3
167	HPS 41	5 41 49.81	−1 56 27.2	15.12	13.19	12.28	7.17±0.32	1.92	3.74±0.17	85± 1.3
168	HPS 42	5 41 52.93	−1 56 29.6	18.00	14.78	12.87	25.17±0.57	3.07	8.20±0.19	89± 0.7
169	—	5 41 54.98	−1 56 31.2	16.62	13.53	11.89	8.82±0.16	3.71	2.37±0.04	91± 0.5
170	HPS 43	5 41 52.95	−1 56 35.1	13.68	11.84	11.05	9.69±0.06	1.40	6.91±0.04	97± 0.2
171	—	5 41 59.79	−1 56 36.8	15.86	14.56	13.84	3.81±0.33	1.33	2.87±0.25	91± 2.4
172	—	5 41 43.45	−1 56 42.6	15.43	12.52	11.23	8.12±0.07	2.80	2.90±0.02	106± 0.2
173	HPS 44	5 41 53.41	−1 56 48.1	15.71	14.22	13.27	4.20±0.28	0.79	5.31±0.35	96± 1.9
174	HPS 45	5 41 54.92	−1 56 48.3	14.26	12.66	11.76	7.16±0.07	1.83	3.92±0.04	92± 0.3
175	—	5 41 50.57	−1 56 52.4	16.34	14.42	13.29	3.35±0.38	1.41	2.37±0.27	68± 3.2
176	—	5 41 35.85	−1 57 12.2	15.58	12.62	11.21	7.13±0.13	3.21	2.23±0.04	115± 0.5
177	HPS 46	5 41 52.33	−1 57 12.2	15.74	14.33	13.52	8.20±0.30	1.61	5.10±0.18	94± 1.0
178	—	5 41 45.05	−1 57 13.2	17.36	16.73	16.25	7.49±1.81	0.00	—	3± 6.7
179	HPS 47	5 41 52.16	−1 57 17.4	12.97	11.19	10.27	7.56±0.03	1.90	3.98±0.01	107± 0.1
180	HPS 48	5 41 44.96	−1 57 17.5	13.84	13.23	12.94	1.26±0.07	0.28	4.56±0.27	105± 1.7
181	HPS 49	5 41 54.72	−1 57 27.3	12.88	11.74	11.29	5.21±0.03	0.71	7.35±0.04	91± 0.1
182	HPS 50	5 41 38.61	−1 57 30.1	13.85	12.44	11.79	7.31±0.07	1.29	5.69±0.05	110± 0.3
183	HPS 51	5 41 50.04	−1 57 30.6	13.43	11.96	11.28	4.50±0.04	1.33	3.39±0.03	74± 0.2
184	—	5 41 45.62	−1 57 33.1	14.19	13.45	12.92	2.14±0.10	0.00	—	102± 1.4
185	HPS 52	5 41 44.20	−1 57 35.3	15.43	13.47	12.43	9.71±0.15	2.18	4.45±0.07	90± 0.4
186	HPS 53	5 41 44.51	−1 57 40.2	13.78	11.75	10.84	6.56±0.03	1.80	3.64±0.02	100± 0.1
187	HPS 54	5 41 36.56	−1 57 41.3	15.41	13.19	12.18	8.28±0.19	1.99	4.16±0.10	108± 0.7
188	HPS 55	5 41 53.19	−1 57 43.9	12.78	11.09	10.06	7.18±0.02	1.07	6.71±0.02	105± 0.1
189	—	5 41 30.82	−1 57 44.1	16.00	15.48	15.39	1.55±1.36	0.00	—	170±18.9
190	HPS 56	5 41 35.49	−1 57 44.7	14.12	13.48	13.26	1.41±0.18	0.17	8.36±1.08	110± 3.7
191	—	5 41 50.15	−1 57 44.8	13.87	11.74	10.50	5.09±0.06	1.72	2.96±0.04	127± 0.4
192	—	5 41 32.57	−1 57 49.8	17.86	15.69	14.75	3.67±1.83	1.82	2.01±1.00	103±12.8
193	HPS 57	5 41 53.71	−1 57 50.2	15.87	14.35	13.45	6.07±0.36	0.89	6.84±0.40	108± 1.7
194	—	5 41 41.65	−1 57 54.6	12.47	10.32	9.05	1.50±0.02	1.70	0.88±0.01	85± 0.3
195	—	5 41 31.48	−1 57 57.0	16.45	14.77	13.97	3.58±0.74	1.65	2.17±0.45	109± 5.8
196	—	5 41 32.75	−1 57 57.3	12.29	11.54	11.36	1.46±0.04	0.00	—	109± 0.7
197	—	5 41 32.39	−1 57 58.5	17.81	16.26	15.58	<2.31	1.22	<1.89	21±30.2
198	—	5 41 59.01	−1 58 01.2	17.53	14.96	13.73	3.35±0.47	2.74	1.22±0.17	118± 4.0
199	HPS 58	5 41 50.62	−1 58 04.1	14.29	13.37	12.79	3.45±0.09	0.12	29.80±0.76	88± 0.7
200	—	5 41 50.06	−1 58 08.1	15.88	15.01	14.53	2.34±0.40	0.73	3.21±0.54	125± 4.8
201	—	5 41 57.75	−1 58 09.9	16.93	15.19	14.40	3.54±0.55	1.60	2.21±0.35	108± 4.4
202	HPS 59	5 41 54.07	−1 58 16.9	13.59	12.71	12.27	2.70±0.05	0.68	3.99±0.07	99± 0.5
203	HPS 60	5 41 38.17	−1 58 17.6	14.16	12.50	11.86	6.32±0.06	1.13	5.61±0.06	106± 0.3
204	HPS 61	5 41 45.34	−1 58 19.0	15.97	15.40	15.14	0.96±0.56	0.21	4.60±2.66	81±14.3
205	—	5 41 47.24	−1 58 20.1	16.85	13.58	11.84	6.46±0.14	3.97	1.63±0.03	94± 0.6
206	—	5 41 43.60	−1 58 22.3	15.37	13.64	12.81	3.44±0.13	1.73	1.98±0.08	107± 1.1
207	HPS 62	5 41 33.14	−1 58 23.9	17.18	15.87	15.13	9.57±1.83	1.38	6.96±1.33	120± 5.4
208‖	—	5 41 52.07	−1 58 32.4	16.42	15.51	14.61	12.58±0.74	—	—	140± 1.7
209	—	5 41 42.03	−1 58 40.3	16.72	14.97	14.19	1.52±0.55	1.52	1.00±0.37	22± 9.8
210	HPS 63	5 41 43.99	−1 58 45.4	14.94	13.41	12.43	3.03±0.14	0.82	3.68±0.17	91± 1.3
211	HPS 64	5 41 41.86	−1 58 48.9	14.06	12.71	11.78	2.62±0.07	0.55	4.79±0.13	103± 0.8

* Source ID of highly polarized sources with $P_H/A_H > 3.38$.
† Equatorial coordinates (J2000.0).
‡ A_H estimated on the two color diagram.
§ Errors are estimated using δP_H.
‖ Protostar candidate.

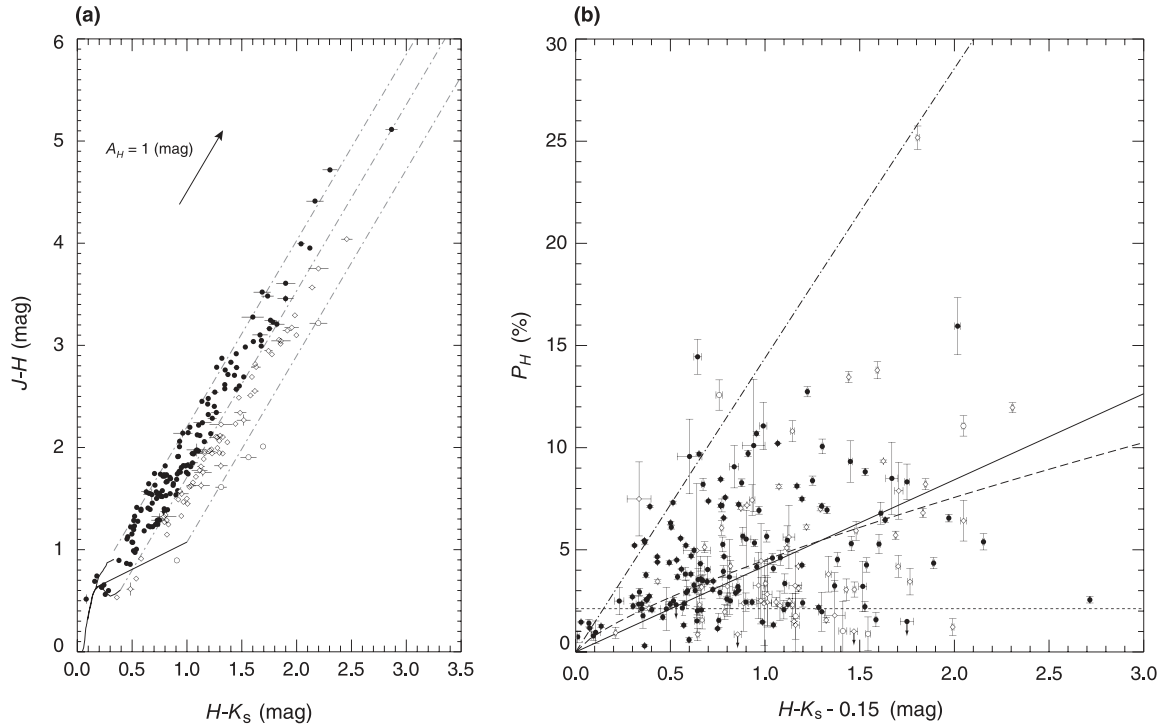

Fig. 6. Left panel: Two color diagram of the stars toward NGC 2024. Filled circles, open diamonds, and open circles denote dwarf+giant stars, PMS stars, and Class I candidates, respectively. The dwarf and giant locus were from Bessell and Brett (1988), and T Tauri locus was from Meyer, Calvet, and Hillenbrand (1997). The reddening vector was calculated using the reddening law from Nishiyama et al. (2006) and transformed from IRSF to 2MASS system. Right panel: $H - K_s - 0.15$ vs. P_H diagram. Dashed and dot-dashed lines are the relationship for interstellar molecular clouds and its upper limit (Jones 1989). Solid line shows the result of linear fitting to all data points. Dotted line shows the mode value of P_H.

Table 3. Fractions of highly polarized sources.

H^* (mag)	Fraction† (%)	Number†	Total number‡
9.5	31 ± 8.9%	12	39
10.5	29 ± 8.2%	12	42
11.5	31 ± 9.5%	11	35
12.5	36 ± 11.3%	10	28
13.5	39 ± 13.0%	9	23

* Dereddened H magnitudes. Each bin is separated by 1 mag.
† The fraction and the number of stars with $P_H/A_H > 3.38$ in each bin.
‡ Total number of stars in each bin.

by the disk lifetime.

Theoretically, very low-mass stars (i.e., brown dwarfs) are expected to have a more flared (larger scale height) disk than those for more massive stars due to its small gravity (Walker et al. 2004). Highly flared disks result in a large fraction of obscured stars due to extinction, so that only scattered light is observed, making the source an HPS. Considering the disk optical depth (i.e., size and mass) and its flaring for several models, the disk obscuring probability of brown dwarfs in the K band (2.2μm) was estimated to be larger than that for Class II stars by a factor of $\sim$ 1–3 (Walker et al. 2004). Thus, a stellar mass dependence of HPS detection rate may be observed.

To derive intrinsic luminosities, we performed dereddening of stars by subtracting A_H from the observed H magnitudes. We then derived the fraction of sources with $P_H/A_H > 3.38$ against the dereddened H mag at each bin separated by 1 mag. The result is given in table 3. Note that stars with $H \geq 13.3$ mag are brown dwarfs at the employed distance of 415 pc (Anthony-Twarog 1982). We found that the distribution of the polarization fraction remains constant from low luminosity (brown dwarfs) to higher luminosity (solar-type) stars, although the error in the polarization fraction is not small. According to the argument above, our finding suggests that the dependence of the disk scale height on the mass of the central star is not significant in spite of the theoretical model that predicts more flared disks for lower mass stars. It is noteworthy that a very similar result was obtained in the OMC-1 region (N. Kusakabe et al. in preparation). Quantitative studies on the origin of flat HPS distributions will be discussed in a later paper.

Recently, Levine et al. (2006) reported spectroscopic studies of low-mass stars and brown dwarfs distributed over a $10' \times 10'$ region in NGC 2024. Their list of 71 stars with known spectral type can be more useful to investigate the relationship between the stellar mass and P_H/A_H. We matched the coordinates of their sources with our polarimetry, and found 49 pairs. We show the stellar mass versus P_H/A_H diagram in figure 8. The vertical and horizontal broken lines denote the upper limit of the brown-dwarf mass (0.08 $M_\odot$) and $P_H/A_H = 3.38$,

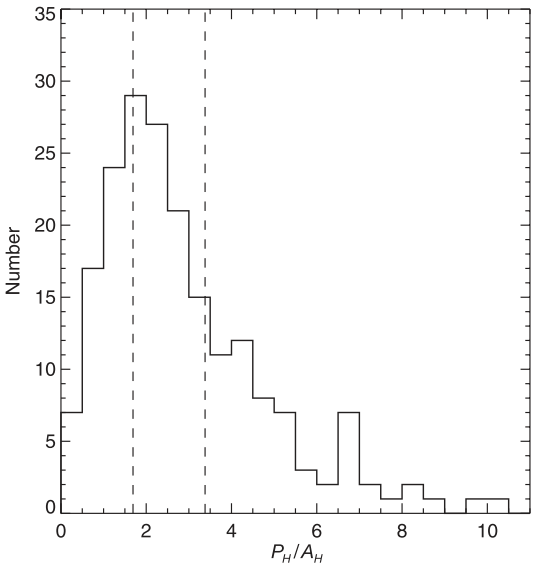

Fig. 7. Histogram of P_H/A_H for all the stars except for protostar candidates. The dashed line on the left side shows $P_H/A_H = 1.69$, which corresponds to the solid line in figure 6b. The dashed line on the right side shows $P_H/A_H = 3.38$.

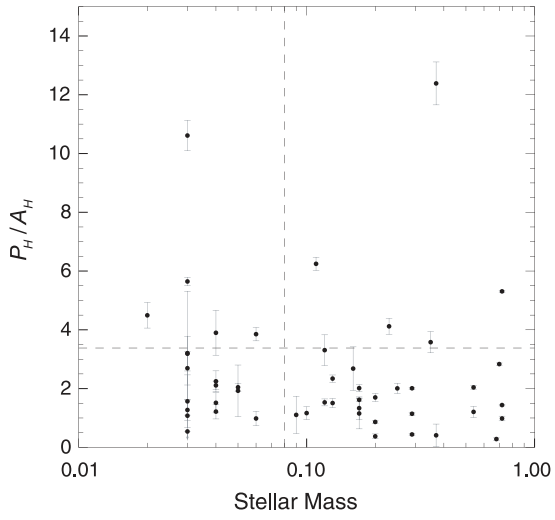

Fig. 8. Relationship between stellar mass and P_H/A_H in NGC 2024. The value of the stellar mass was taken from Levine et al. (2006). The mass range covers from brown dwarfs to solar-type stars. The vertical and horizontal broken lines denote the upper limit of brown dwarf mass (0.08 $M_\odot$) and $P_H/A_H = 3.38$, respectively.

respectively. It is clear that there is no obvious tendency for higher P_H/A_H valves for lower mass stars. If we divide the sources into two groups at the line of $M = 0.08 M_\odot$, the median P_H/A_H value with $(\mathrm{rms})/\sqrt{n}$ error is 2.11 ± 0.53 and 1.62 ± 0.43 for the lower and higher mass groups, respectively. There can be a tendency of slightly higher P_H/A_H for brown dwarfs than that for solar-type stars, but, within $1\,\sigma$, those two values are identical. We should also note the difference in the suffered mean extinction for both groups is small ($\langle A_H \rangle_{\mathrm{brown\ dwarf}} = 1.5$ mag and $\langle A_H \rangle_{\mathrm{solar\text{-}type}} = 1.9$ mag). We conclude that the stellar mass vs. P_H/A_H relationship is generally flat in the mass range from brown dwarfs to solar-type stars.

In figure 8, the sources located above the horizontal broken line can be classified as HPS. Their properties are summarized in table 4.[2] We found ten HPSs that consist of five brown dwarfs and five low-mass stars. It is most likely that these sources are associated with circumstellar materials that produce highly polarized light through dust scattering. The existence of a circumstellar disk around young brown dwarfs has been indirectly suggested (e.g., infrared excess emission, Muench et al. 2001). In addition to a few samples revealed by the imaging of disks using HST (Bally et al. 2000) and outflow detection with spectro-astrometry (Whelan et al. 2005), our five samples serve as "direct" evidence for the existence of a disk/envelope system around brown dwarfs (see also, Tamura et al. 2006; N. Kusakabe et al. in preparation).

3.3.3. Magnetic field structure

The aperture polarimetry of stars provides important information on the direction of magnetic fields. If we assume the normal grains alignment, i.e., the spin axis of elongated dust grains align parallel to the magnetic fields (Davis & Greenstein 1951), the direction of magnetic fields projected onto the sky can be inferred from the direction of the polarization vectors of stars ($B \parallel E$, e.g., Weintraub et al. 2000). Though a grain alignment mechanism caused by gas streaming motion (Gold 1952) may be the dominant process near or around sources with molecular outflows, we believe our assumption is plausible, because we discuss the structure of magnetic fields not only around each outflow source, but also across the entire surface of NGC 2024.

In figure 9, we show a histogram of the polarization position angle, θ_H, of stars in NGC 2024. It is clear that the stars with $P_H \geq 3\%$ show a peak at a position angle of 110°. The large-scale distribution of the magnetic field in NGC 2024 is thus expected to be in the direction of 110°. In the right panel, the stars with low polarization ($P_H < 3\%$) show a less-clear tendency. In the histogram, we show the numbers of protostars, PMS stars, and dwarf+giant stars in dark gray, gray, and white colors, respectively. There is no large difference in the shape of histograms among three groups with different evolutionary stages.

We show the distribution of polarization vectors for each star in figure 10. Though the overall distribution of the polarization angle is $\sim 110°$, we found a bend of the magnetic fields around the northwest of the star-forming ridge of NGC 2024. Since the bend of the magnetic field orientation is localized on the polarization map, it is most likely that the structure is not associated with ambient material around NGC 2024, but is associated with a smaller-scale structure inside the region, i.e., the star-forming ridge.

Matthews, Fiege, and Moriarty-Schieven (2002) studied the magnetic field structure of NGC 2024 based on sub-mm dust continuum observations using the polarimetry mode of JCMT/SCUBA. We overlaid the polarization vector of stars on

[2] Full listing of all sources is supplied in the table attached with the electric version: ⟨http://pasj.asj.or.jp/v59/n3/59⟩

Table 4. Highly polarized sources with known spectral type.

Star name*	P_H† (%)	A_H* (mag)	P_H/A_H (% mag^{-1})	θ_H† (°)	M subclass*	Mass* ($M_\odot$)
FLMN_J0541328−0151271 (57)‡	4.22±0.41	0.94	4.49±0.43	147±2.8	8.50	0.02
FLMN_J0541506−0158041 (25)	3.45±0.09	0.61	5.65±0.14	88±0.7	7.75	0.03
FLMN_J0541456−0157332 (29)	2.14±0.10	0.20	10.61±0.52	102±1.4	8.00	0.03
FLMN_J0541497−0156198 (55)‡	19.88±3.89	5.10	3.90±0.76	79±5.5	7.00	0.04
FLMN_J0541537−0157503 (52)	6.07±0.36	1.58	3.85±0.23	108±1.7	6.50	0.06
FLMN_J0541523−0157123 (46)	8.20±0.30	1.31	6.25±0.22	94±1.0	5.75	0.11
FLMN_J0541534−0156482 (51)	4.20±0.28	1.02	4.12±0.27	96±1.9	4.00	0.23
FLMN_J0541314−0154347 (30)	7.43±0.75	2.08	3.58±0.36	130±2.9	3.25	0.35
FLMN_J0541357−0153483 (61)	14.45±0.85	1.17	12.39±0.73	112±1.7	2.75	0.37
FLMN_J0541344−0154409 (02)	4.40±0.03	0.83	5.31±0.04	109±0.2	1.75	0.72

* Taken from table 3 of Levine et al. (2006). The numbers in parentheses of column 1 denote the source serial number in their catalog. A_H was calculated by dividing originally cataloged A_V by a factor 5.71.
† This work.
‡ Not cataloged in table 2 but have available P_H measurements.

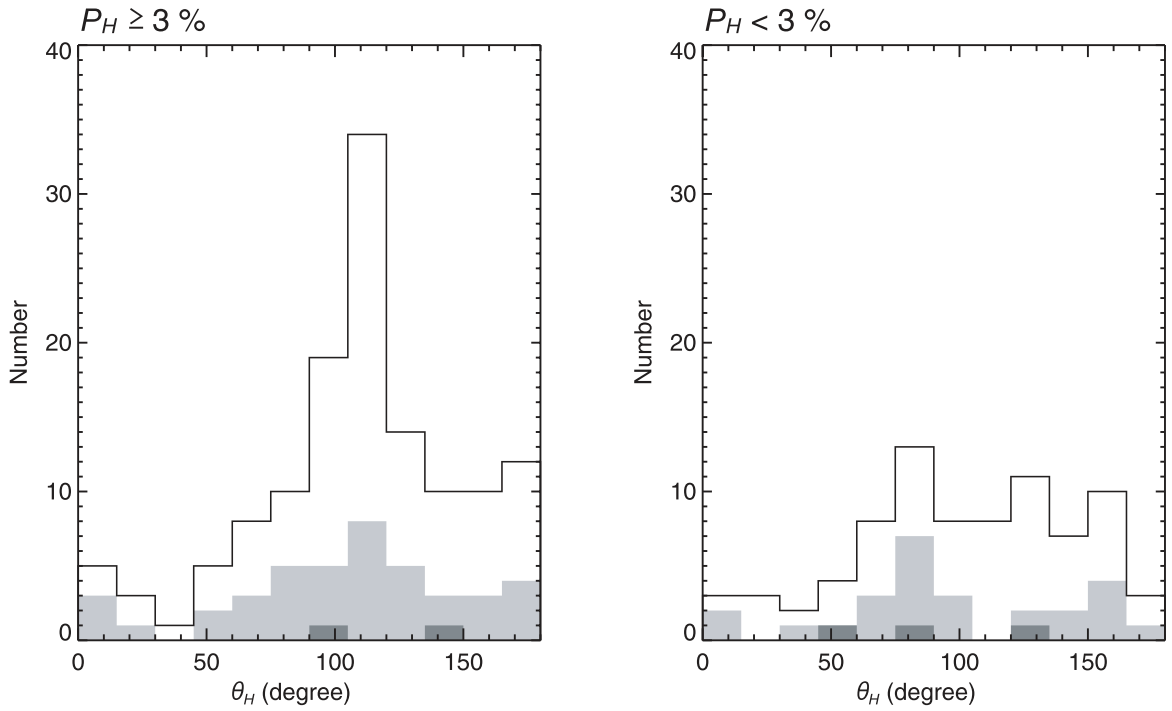

Fig. 9. Histograms of θ_H for the stars with $P_H \geq 3\%$ (left panel) and $P_H < 3\%$ (right panel). The dark-gray, light-gray, and white colors show the number of protostar candidates, PMS stars, and dwarf+giant stars, respectively.

their polarization map, as shown in figure 11. Vectors from the sub-mm emission polarimetry (blue lines) were rotated by 90° so as to be compared with the E-vector of dichroic polarization in the H band (yellow lines). We futher plotted rotated (90°) polarization vectors taken with 100 μm dust emission (red lines, Hildebrand et al. 1995; Dotson et al. 2000). The background image in figure 11 is a 850 μm dust continuum intensity map taken with JCMT/SCUBA. The gray broken line shows the contour of 0.9 Jy beam^{-1}, which corresponds to $A_V \sim 50$ mag when we use a dust opacity of $\kappa_{850\,\mu\mathrm{m}} = 0.02$ cm^2 g^{-1} and a dust temperature of $T_\mathrm{d} = 18$ K. The region enclosed by the gray broken line is too highly obscured to be traced at near-infrared wavelengths.

We found that the direction of the magnetic field obtained from both dust emission (blue and red lines) and extinction (yellow lines) is generally consistent with each other in the region around and outside of the contour of $A_V \sim 50$ mag. The agreement between the dichroic and dust emission polarizations suggests that the dichroic polarization traces well the magnetic field structure if the lying dense dusty material

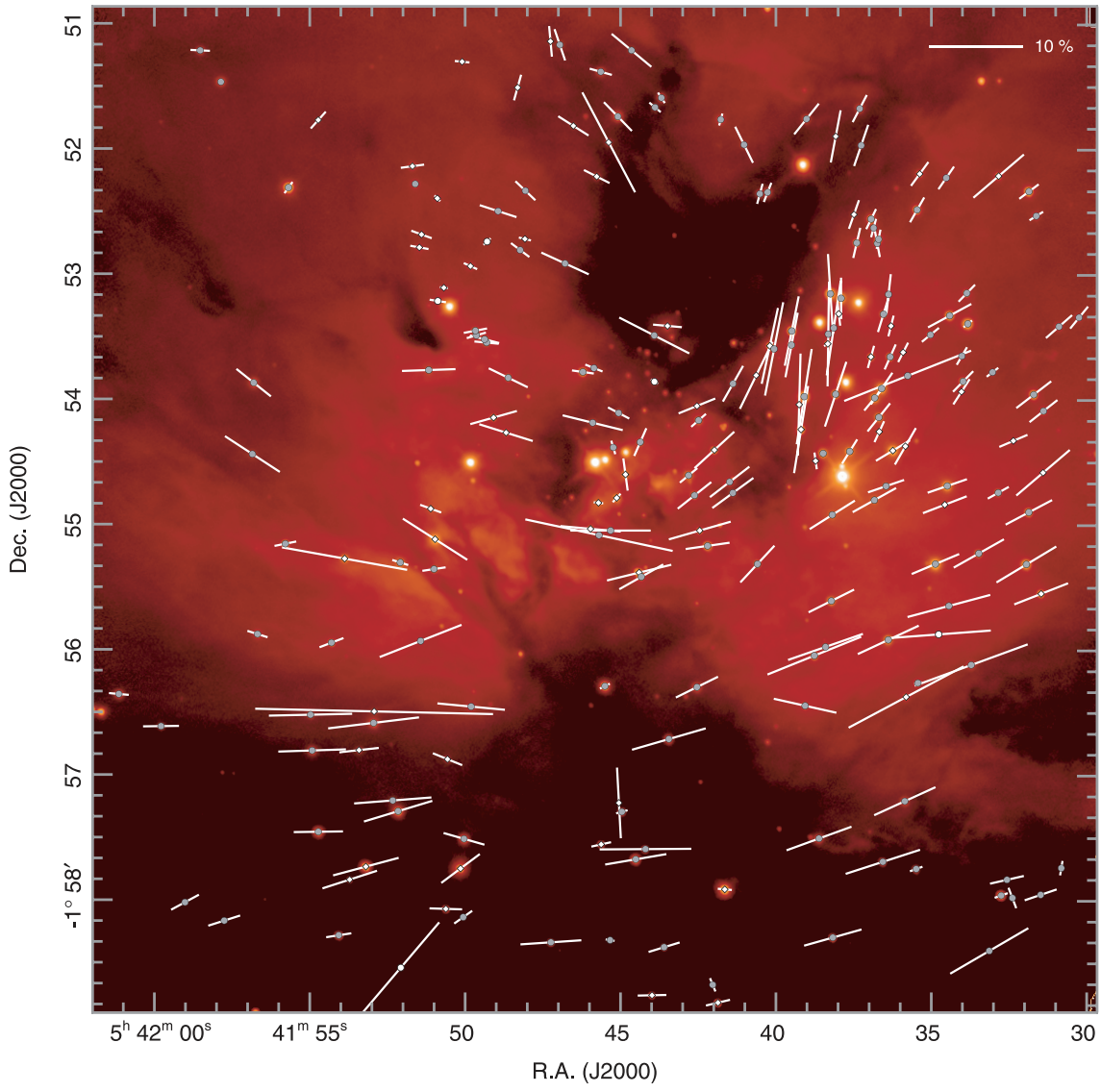

Fig. 10. Polarization vector of each stellar source on H intensity image. The filled gray circles, open diamonds, and open circles denote dwarf+giant stars, PMS stars, and protostar candidates, respectively.

is less than, or as much as, its penetration depth. On the other hand, the dichroic polarization vectors do not show a good correlation with those obtained from dust emission inside the contour of $A_V \sim 50$ mag. It is a natural result if we consider that the dichroic polarization in the H band only traces the magnetic field foreground to the star-forming ridge. The disagreement between the dichroic and dust emission polarizations suggests that the magnetic field structure toward the star-forming ridge, traced using dust emission polarimetry, is localized in both the plane-of-sky and the line-of-sight direction. We note that the line-of-sight variation in the magnetic field strength ($B_{\parallel}$) toward the star-forming ridge was also observed by Crutcher et al. (1999) based on measurements of the Zeeman splitting of the absorption lines of H I and OH with Very Large Array (VLA). On the basis of the sub-mm dust emission polarimetry data, Matthews, Fiege, and Moriarty-Schieven (2002) explained the magnetic field structure toward the star-forming ridge using two different models: one was helical magnetic fields surrounding a curved filamentary cloud; the other was magnetic fields swept by the ionization front of the expanding H II region. It is hard to differentiate the two models based on our near-infrared dichroic polarization data, because the data can not trace the dense region ($A_V \gtrsim 50$ mag) of the star-forming ridge.

It is noteworthy that our result is contrary to the view that the polarization of background starlight in the optical to near-infrared wavelengths does not trace magnetic fields (i.e., grain alignment) inside cold and dense molecular clouds (e.g., Goodman et al. 1995). For example, Arce et al. (1998) suggested that the dichroic polarization of background stars toward the Taurus dark cloud only trace the region up to $A_V \sim 1.3$ mag, indicating that the dichroic polarization does not trace the magnetic field inside cold dark clouds, due to a significant depolarization effect. Their criticism may not be the case for other star-forming regions where the environment is different

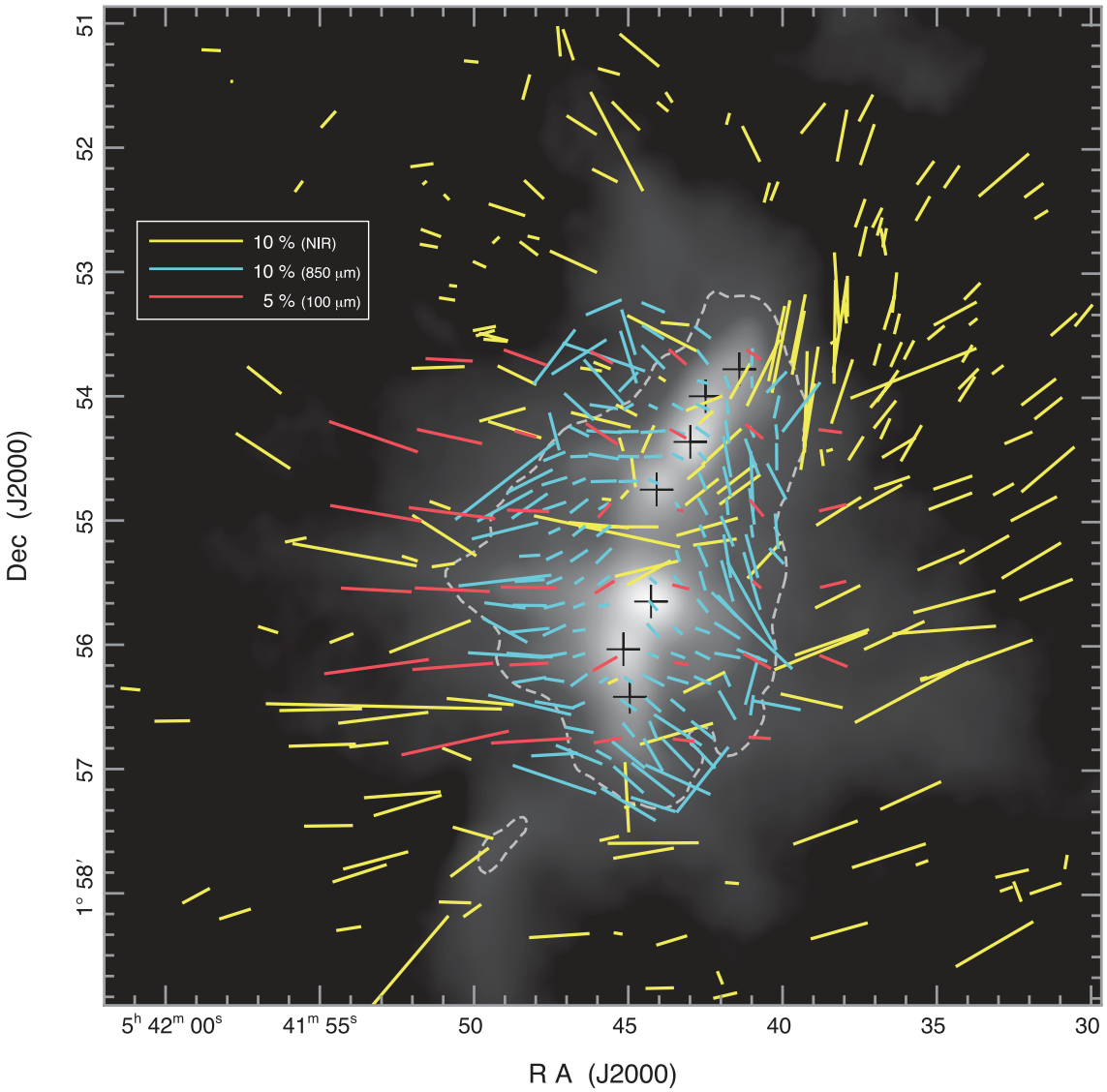

Fig. 11. Polarization vectors obtained through the near-infrared polarimetry at H (yellow, this work), dust emission polarimetry at 850 μm (blue, Matthews et al. 2002), and at 100 μm (red, Hildebrand et al. 1995; Dotson et al. 2000). Vectors from the dust emission polarimetry were rotated by 90° for the comparison with the E-vector of dichroic polarization (inferred direction of magnetic field). The background image is the 850 μm dust continuum intensity map (logarithmic scale) kindly provided by Doug Johnstone. The contour of gray broken line denote the level of 0.9 Jy beam^{-1}. Plus symbols denote far-infrared sources, FIR 1–7 from north to south, reported by Mezger et al. (1988, 1992).

(e.g., higher temperature[3]) from those in cold dark clouds. In addition to the NGC 2024 region, a good consistency in the magnetic field structure obtained using dichroic polarization and dust continuum polarization is confirmed in the OMC-1 (Houde et al. 2004; N. Kusakabe et al. in preparation) and NGC 2071 (Matthews et al. 2002; Tamura et al. 2006) region. We thus conclude that the dichroic polarization at near-infrared wavelengths is a better tracer of magnetic field structures than previously thought, and that wide-field near-infrared polarimetry is useful to reveal the magnetic field structures in various star-forming regioins.

[3] The temperature of gas and dust was measured as $T_{\rm kin} \lesssim 20$ K (Gaume et al. 1992; Mauersberger et al. 1992) and $T_{\rm d} \sim 16$–18K (16 K toward the star-forming ridge: Mezger et al. 1988; 18 K toward the Orion B South region: Johnstone et al. 2006) in NGC 2024.

4. Summary

We conducted deep and wide-field $JHK_{\rm s}$ imaging polarimetry toward NGC 2024, a massive star-forming region in the Orion B cloud. This was the first imaging polarimetry covering the H II region as well as embedded young cluster in NGC 2024. Our conclusions are summarized as follows:

1. We found a prominent and extended infrared reflection nebula (IRN) over NGC 2024 on our polarization images. We constrained the location of the illuminating source of the nebula through an analysis of the polarization vectors. A massive star, IRS 2b with a spectral type of O8–B2, is located at the center of the symmetric vector pattern.
2. We discovered five small-scale IRNe associated with

YSOs in our polarization images. The pattern of the polarization vector around the stars appears to be centrosymmetric, indicating that these IRNe are illuminated by each central star, and are responsible for the structure of circumstellar material that produces strongly polarized light through dust scattering. The polarized intensity of each IRN shows a butterfly-shaped emission pattern extending over 5000–10000 AU, which agrees well with the picture of a disk/envelope system around young stars.

3. We performed software aperture polarimetry of the 211 point-like sources detected on the Stokes I images at JHK_s. We cataloged 64 highly polarized sources (HPS) as candidates associated with circumstellar material by selecting sources with stronger polarizations than estimated from dichroic extinction.
4. We investigated the fraction of highly polarized sources against the intrinsic luminosity of stars ($\propto$ mass), and found that the source detection rate remains constant from low (brown dwarfs) to higher luminosity (solar-type) stars. Since most stars in the region are young enough to have circumstellar disks, possible differences in disk lifetime should not affect our statistics. Though a stellar-mass-dependence of disk scale height (flaring) is a possible factor to naturally change the detection rate of highly polarized source, our result indicates that the effect is not significant in spite of the theoretical prediction of more flared disks for lower mass stars. We confirmed the result using our polarimetry of the stars with known spectral types toward NGC 2024..
5. By comparing our polarimetry with the spectrophotometry by Levine et al. (2006), we found five brown dwarfs with highly polarized integrated emission. These sources serve as direct evidence of circumstellar material around brown dwarfs.
6. We investigated the magnetic field structure of NGC 2024 through the measurements of dichroic polarization of point sources. The position angle of projected magnetic field across the region is found to be 110°. We also found a bending of magnetic fields around the northwest of the star-forming ridge of NGC 2024.
7. In the region of $A_V \leq 50$ mag, we found good consistency in magnetic field structures obtained using dichroic polarization at near-infrared and dust continuum polarization at sub-mm/far-infrared wavelengths. Similar results are also found in the OMC-1 and NGC 2071 regions. These results strongly indicate that the dichroic polarization at near-infrared wavelengths traces the magnetic field structures inside dense molecular clouds.
8. In the region of $A_V > 50$ mag over the star-forming ridge, the dichroic polarization does not show good correlation with those obtained from dust emission. It is a natural result if we consider that the dichroic polarization at near-infrared wavelengths can only trace the alignment of foreground dust. The disagreement between the dichroic and dust emission polarizations suggests that the magnetic field structure toward the star-forming ridge traced using dust emission polarimetry is localized in both the plane-of-sky and the line-of-sight directions.

We are grateful to Shuji Sato and Phil Lucas for their helpful comments and suggestions. Thanks are due to the staff in SAAO for their kind help during the observations. We thank the referee, Munetaka Ueno, for useful comments on the manuscript. We also thank Doug Johnstone for providing his JCMT/SCUBA data of NGC 2024. The IRSF/SIRIUS project was initiated and supported by Nagoya University, National Astronomical Observatory of Japan, and The University of Tokyo in collaboration with South African Astronomical Observatory under a financial support of Grants-in-Aid for Scientific Research on Priority Area (A) No. 10147207 and No. 10147214, and Grants-in-Aid No. 13573001 and No. 16340061 of the Ministry of Education, Culture, Sports, Science, and Technology of Japan. M. T. and R. K. acknowledges support by the Grants-in-Aid (Nos. 16077101, 16077204, 16340061). J. H. acknowledges support by PPARC.

References

Anthony-Twarog, B. J. 1982, AJ, 87, 1213
Arce, H. G., Goodman, A. A., Bastien, P., Manset, N., & Sumner, M. 1998, ApJ, 499, L93
Bally, J., O'Dell, C. R., & McCaughrean, M. J. 2000, AJ, 119, 2919
Barnes, P. J., Crutcher, R. M., Bieging, J. H., Storey, J. W. V., & Willner, S. P. 1989, ApJ, 342, 883
Bessell, M. S., & Brett, J. M. 1988, PASP, 100, 1134
Bik, A., Lenorzer, A., Kaper, L., Comerón, F., Waters, L. B. F. M., de Koter, A., & Hanson, M. M. 2003, A&A, 404, 249
Chandler, C. J., & Carlstrom, J. E. 1996, ApJ, 466, 338
Cohen, M. 1994, AJ, 107, 582
Crutcher, R. M., Henkel, C., Wilson, T. L., Johnston, K. J., & Bieging, J. H. 1986, ApJ, 307, 302
Crutcher, R. M., Roberts, D. A., Troland, T. H., & Goss, W. M. 1999, ApJ, 515, 275
Cutri, R. M., et al. 2003, 2MASS All-Sky Catalog of Point Sources (Pasadena: Caltech)
Davis, L., Jr., & Greenstein, J. L. 1951, ApJ, 114, 206
Dotson, J. L., Davidson, J., Dowell, C. D., Schleuning, D. A., & Hildebrand, R. H. 2000, ApJS, 128, 335
Gaume, R. A., Johnston, K. J., & Wilson, T. L. 1992, ApJ, 388, 489
Gold, T. 1952, MNRAS, 112, 215
Goodman, A. A., Jones, T. J., Lada, E. A., & Myers, P. C. 1995, ApJ, 448, 748
Grasdalen, G. L. 1974, ApJ, 193, 373
Haisch, K. E., Jr., Lada, E. A., & Lada, C. J. 2000, AJ, 120, 1396
Haisch, K. E., Jr., Lada, E. A., Piña, R. K., Telesco, C. M., & Lada, C. J. 2001, AJ, 121, 1512
Heckert, P. A., & Zeilik, M., II 1981, AJ, 86, 1076

Hildebrand, R. H., Dotson, J. L., Dowell, C. D., Platt, S. R., Schleuning, D., Davidson, J. A., & Novak, G. 1995, in ASP Conf. Ser. 73, Airborne Astronomy Symposium on the Galactic Ecosystem: From Gas to Stars to Dust, ed. M. R. Haas, J. A. Davidson, & E. F. Erickson (San Francisco: ASP), 97
Hodapp, K. W. 1984, A&A, 141, 255
Houde, M., Dowell, C. D., Hildebrand, R. H., Dotson, J. L., Vaillancourt, J. E., Phillips, T. G., Peng, R., & Bastien, P. 2004, ApJ, 604, 717
Johnstone, D., Matthews, H., & Mitchell, G. F. 2006, ApJ, 639, 259
Jones, T. J. 1989, ApJ, 346, 728
Jones, T. J., Klebe, D., & Dickey, J. M. 1992, ApJ, 389, 602
Kandori, R., et al. 2006, Proc. SPIE, 6269, 159
Kruegel, E., Thum, C., Pankonin, V., & Martin-Pintado, J. 1982, A&AS, 48, 345
Lada, E. A., 1999, in The Origin of Stars and Planetary Systems, ed. C. J. Lada & N. D. Kylafis (Dordrecht: Kluwer), 441
Lada, E. A., Evans, N. J., II, Depoy, D. L., & Gatley, I. 1991, ApJ, 371, 171
Levine, J. L., Steinhauer, A., Elston, R. J., & Lada, E. A. 2006, ApJ, 646, 1215
Matthews, B. C., Fiege, J. D., & Moriarty-Schieven, G. 2002, ApJ, 569, 304
Mauersberger, R., Wilson, T. L., Mezger, P. G., Gaume, R., & Johnston, K. J. 1992, A&A, 256, 640
Meyer, M. R. 1996, Ph.D. thesis, Univ. of Massachusetts
Meyer, M. R., Calvet, N., & Hillenbrand, L. A. 1997, AJ, 114, 288
Mezger, P. G., Chini, R., Kreysa, E., Wink, J. E., & Salter, C. J. 1988, A&A, 191, 44
Mezger, P. G., Sievers, A. W., Haslam, C. G. T., Kreysa, E., Lemke, R., Mauersberger, R., & Wilson, T. L. 1992, A&A, 256, 631
Moore, T. J. T. & Chandler, C. J. 1989, MNRAS, 241, 19
Moore, T. J. T., & Yamashita, T. 1995, ApJ, 440, 722
Muench, A. A., Alves, J., Lada, C. J., & Lada, E. A. 2001, ApJ, 558, 51
Nagata, T., Sato, S., & Kobayashi, Y. 1983, A&A, 119, 1
Nagayama, T., et al. 2003, Proc. SPIE, 4841, 459
Nishiyama, S., et al. 2006, ApJ, 638, 839
Sato, S., Nagata, T., Nakajima, T., Nishida, M., Tanaka, M., & Yamashita, T. 1985, ApJ, 291, 708
Stetson, P. B. 1987, PASP, 99, 191
Strom, S. E., Edwards, S., & Skrutskie, M. F. 1993, in Protostars and Planets III, ed. E. H. Levy & J. I. Lunine (Tucson: Univ. Arizona Press), 837
Tamura, M., et al. 2006, ApJ, 649, 29
Tamura, M., et al. 2007, PASJ, 59
Wainscoat, R. J., Cohen, M., Volk, K., Walker, H. J., & Schwartz, D. E. 1992, ApJS, 83, 111
Walker, C., Wood, K., Lada, C. J., Robitaille, T., Bjorkman, J. E., & Whitney, B. 2004, MNRAS, 351, 607
Wardle, J. F. C., & Kronberg, P. P. 1974, ApJ, 194, 249
Weintraub, D. A., Goodman, A. A., & Akeson, R. L. 2000, in Protostars and Planets IV, ed. V. Mannings, A. P. Boss, & S. S. Russell (Tucson: Univ. Arizona Press), 247
Whelan, E. T., Ray, T. P., Bacciotti, F. Natta, A. Testi, L., & Randich, S. 2005, Nature, 435, 652
Whittet, D. C. B. 1992, in Dust in the Galactic Environment (Piladelphia: Inst. Phys.)
Wilking, B. A., Lebofsky, M. J., Kemp, J. C., Martin, P. G., & Rieke, G. H. 1980, ApJ, 235, 905